



HAL
open science

Astrocytes mediate oxytocin's effect on central amygdala circuitry that regulates emotional behavior in rodents

Jérôme Wahis, Angel Baudon, Ferdinand Althammer, Damien Kerspern, Stéphanie Goyon, Daisuke Hagiwara, Arthur Lefevre, Lara Barteczko, Benjamin Boury-Jamot, Benjamin Bellanger, et al.

► To cite this version:

Jérôme Wahis, Angel Baudon, Ferdinand Althammer, Damien Kerspern, Stéphanie Goyon, et al.. Astrocytes mediate oxytocin's effect on central amygdala circuitry that regulates emotional behavior in rodents. *Nature Neuroscience*, 2021, 24, pp.529-541. 10.1038/s41593-021-00800-0 . hal-03178553v1

HAL Id: hal-03178553

<https://hal.science/hal-03178553v1>

Submitted on 21 Sep 2021 (v1), last revised 23 Mar 2021 (v2)

HAL is a multi-disciplinary open access archive for the deposit and dissemination of scientific research documents, whether they are published or not. The documents may come from teaching and research institutions in France or abroad, or from public or private research centers.

L'archive ouverte pluridisciplinaire **HAL**, est destinée au dépôt et à la diffusion de documents scientifiques de niveau recherche, publiés ou non, émanant des établissements d'enseignement et de recherche français ou étrangers, des laboratoires publics ou privés.

1 **Astrocytes mediate oxytocin's effect on central amygdala circuitry that regulates**
2 **emotional behavior in rodents**
3

4 Jérôme Wahis^{1,†,§}, Angel Baudon^{1,†}, Ferdinand Althammer^{2,†}, Damien Kerspern^{1,†}, Stéphanie
5 Goyon¹, Daisuke Hagiwara³, Arthur Lefevre^{1,3}, Lara Barteczko³, Benjamin Boury-Jamot⁴,
6 Benjamin Bellanger¹, Marios Abatis⁴, Miriam Silva da Gouveia⁵, Diego Benusiglio³, Marina
7 Eliava³, Andrej Rozov⁶, Ivan Weinsanto¹, Hanna Sophie Knobloch-Bollmann^{7,§}, Matthew K.
8 Kirchner², Ranjan K. Roy², Hong Wang^{8,§}, Marie Pertin⁹, Perrine Inquimbert¹, Claudia
9 Pitzer¹⁰, Jan Siemens⁸, Yannick Goumon¹, Benjamin Boutrel⁴, Christophe Maurice Lamy¹¹,
10 Isabelle Decosterd^{9,12}, Jean-Yves Chatton⁹, Nathalie Rouach¹³, Scott W. Young¹⁴, Javier E.
11 Stern², Pierrick Poisbeau¹, Ron Stoop⁴, Pascal Darbon¹, Valery Grinevich^{3,#,*}, Alexandre
12 Charlet^{1,15,#,*}
13

14 ¹ Centre National de la Recherche Scientifique and University of Strasbourg, UPR3212
15 Institute of Cellular and Integrative Neurosciences, Strasbourg, France. ² Center for
16 Neuroinflammation and Cardiometabolic Diseases, Georgia State University, Atlanta, USA. ³
17 Department of Neuropeptide Research for Psychiatry, Central Institute of Mental Health,
18 University of Heidelberg, Mannheim, Germany. ⁴ Center for Psychiatric Neurosciences,
19 Hôpital de Cery, Lausanne University Hospital (CHUV), Lausanne, Switzerland. ⁵ German
20 Cancer Research Center (DKFZ), Heidelberg, Germany, ⁶ OpenLab of Neurobiology, Kazan
21 Federal University, Kazan, Russia, Federal Center of Brain Research and
22 Neurotechnologies, Moscow, Russia and Department of Physiology and Pathophysiology,
23 University of Heidelberg, Heidelberg, Germany. ⁷ Department of Molecular and Cellular
24 Biology, Center for Brain Science, Harvard University, Cambridge, USA[§]. ⁸ Department of
25 Pharmacology, Heidelberg University, Heidelberg, Germany[§]. ⁹ Pain center, Department of
26 Anesthesiology, Lausanne University Hospital (CHUV), Lausanne, Switzerland. ¹⁰
27 Interdisciplinary Neurobehavioral Core (INBC), Ruprecht-Karls-Universität, Heidelberg. ¹¹
28 Division of Anatomy, Faculty of Medicine, University of Geneva, Geneva, Switzerland. ¹²
29 Department of Fundamental Neurosciences, Faculty of Biology and Medicine (FBM),
30 University of Lausanne, Lausanne, Switzerland. ¹³ Neuroglial Interactions in Cerebral
31 Physiopathology, Center for Interdisciplinary Research in Biology, Collège de France, Centre
32 National de la Recherche Scientifique UMR 7241, Institut National de la Santé et de la
33 Recherche Médicale U1050, Labex Memolife, PSL Research University, Paris, France. ¹⁴
34 Section on Neural Gene Expression, National Institute of Mental Health, National Institutes of
35 Health, Bethesda, MD, USA. ¹⁵ University of Strasbourg Institute for Advanced Study
36 (USIAS), Strasbourg, France. [§]Present addresses: JW: Laboratory of Glia Biology, VIB-KU
37 Leuven Center for Brain and Disease Research, Department of Neuroscience, KU Leuven
38 Brain Institute, Leuven, Belgium. HSKB: Group of Systemic and Cellular Neuroscience,
39 Institute of Physiology, University of Freiburg, Germany. HW: The Brain Cognition and Brain
40 Disease Institute of Shenzhen Institutes of Advanced Technology, Chinese Academy of
41 Sciences, China.

42 † Equal first author. # senior author. * Corresponding author.
43

44 Corresponding Authors
45

46 Alexandre Charlet, PhD
47 Institute of Cellular and Integrative Neurosciences,
48 INCI CNRS UPR3212

49 8, Allée du Général Rouvillois
50 67000 Strasbourg
51 France
52 Phone: (33) 6070 825 06
53 E-mail: acharlet@unistra.fr

54
55 Valery Grinevich, MD, PhD
56 Department of Neuropeptide Research in Psychiatry
57 Central Institute of Mental Health
58 Medical Faculty Mannheim
59 University of Heidelberg
60 J5, Mannheim, 68159
61 Germany
62 Phone: (49) 621 1703 2995
63 E-mail: valery.grinevich@zi-mannheim.de
64
65
66
67
68

69 **SUMMARY**

70
71 Oxytocin (OT) orchestrates social and emotional behaviors through modulation of neural
72 circuits. In the central amygdala (CeA), the release of OT modulates inhibitory circuits and
73 thereby suppresses fear responses and decreases anxiety levels. Using astrocyte-specific
74 gain- and loss-of-function and pharmacological approaches, we demonstrate that a
75 morphologically distinct subpopulation of astrocytes express OT receptors and mediate
76 anxiolytic and positive reinforcement effects of OT in the CeA of mice and rats. The
77 involvement of astrocytes in OT signaling challenges the long-held dogma that OT acts
78 exclusively on neurons and highlight astrocytes as essential components for modulation of
79 emotional states under normal but also chronic pain conditions.
80

81

82 **INTRODUCTION**

83

84 Oxytocin (OT) is a neuropeptide that acts both as a peripheral neurohormone and a central
85 neuromodulator to modulate key physiological functions, from ion homeostasis to complex
86 social behaviors^{1,2}. Early studies indicated that locally released OT induces morphological
87 and functional changes in both the astroglial and neuronal networks of the hypothalamic
88 nuclei producing the neuropeptide³. Activation of oxytocinergic hypothalamic magnocellular
89 neurons, that project further to virtually all forebrain regions, leads to both synaptic and extra-
90 synaptic OT release in the extra-cellular fluid^{4,5}. This last mode of OT release has the
91 potential to activate virtually every cell type expressing OT receptors (OTR) located in close
92 proximity to the sites of axonal OT release⁵.

93

94 A few studies using either autoradiography on cell cultures derived from rat tissue,
95 immunohistochemistry on CNS sections or knock-in mice models found that not only
96 neurons, but also astrocytes express OTRs⁶⁻⁹. Astrocytes are part of the tripartite synapse

97 and capable to modulate neuronal activity as well as to sense the release of
98 neuromodulators into the neuropil¹⁰. There is now accumulating evidence which demonstrate
99 that astrocytes express receptors for various neuromodulators and actually mediate their
100 neurophysiological effects^{11,12}. Mapping of OTR expression in the rodent brain found it was
101 expressed at high levels in several brain regions⁸, and of interest in this study particularly in
102 the lateral and capsular part (CeL) of the central amygdala (CeA)¹³, albeit the types of cells
103 expressing the OTR in this brain region was never elucidated.

104
105 Functionally, the release of OT in the CeL leads to increased firing of GABA-expressing
106 interneurons^{4,13}. These interneurons inhibit projection neurons in the medial CeA (CeM),
107 which serve as CeA output. OT action in this circuit affects amygdala-related functions,
108 including activity of the autonomous nervous system, fear expression and anxious
109 behaviors^{4,14,15}. Furthermore, the CeA is involved in the pathophysiology of a number of
110 neurological diseases, including neuropathic pain and anxiety^{16,17}, in which both astrocytes¹⁸
111 and the OT system¹⁹ are thought to play a significant role. Therefore, it is crucial to
112 understand how the OT system controls pain and its emotional comorbidities, and if
113 astrocytes are involved in these mechanisms.

114
115 Indeed, a role for astrocytes in the regulation of CeA circuits has already been proven in the
116 CeM²⁰, where astrocyte activity can reduce fear-expression in a fear-conditioning paradigm,
117 a role that is surprisingly similar to the effect of OTR signaling in the CeL⁴. We therefore
118 sought to investigate if CeL astrocytes could also play a role in the OT-mediated regulation of
119 CeA circuits and some of their behavioral correlates.

120
121 Our study shows the expression of oxytocin receptors (OTR) in CeL astrocytes and
122 demonstrates that OT directly acts on CeL astrocytes to gate CeL neurons excitability
123 through N-methyl-D-aspartate receptor (NMDAR) (co-)activation. Further, we found that the
124 astrocyte-mediated OTR signaling underlies the anxiolytic and positive reinforcement effects
125 of OT in the CeA. We thus provide the first evidence that OT drives astrocyte activity and that
126 this effect is an essential part of the OTergic modulation of amygdala neuronal circuits and
127 the behaviors they regulate.

128

129

130 RESULTS

131

132 CeL astrocytes express functional OTRs in rats and mice

133

134 To investigate whether CeA astrocytes express OTRs, we performed fluorescent *in situ*
135 hybridization (FISH) combined with immunohistochemistry on rat CeA sections and found
136 some overlap between OTR mRNA signal and an astrocyte marker, glutamine synthase (GS)
137 (Fig. 1a-b; Extended Data Fig. 1a). Within the rat CeL, $18.6\pm 1.8\%$ of astrocytes and
138 $67.8\pm 3.1\%$ of neurons expressed OTR mRNA (Fig. 1c), with similar results in mice
139 (Extended Data Fig. 1b). Using another astrocyte marker, the aldehyde dehydrogenase 1
140 family member L1 (ALDH1L1), we found a similar proportion of OTR mRNA positive (OTR+)
141 rat astrocytes (Extended Data Fig. 1c). Combining RNAscope for OTR mRNA with a third
142 astrocyte marker (glial fibrillary acidic protein, GFAP), we again found OTR mRNA to be
143 present in mouse astrocytes (Extended Data Fig. 1d). Next, to unequivocally demonstrate
144 that CeL astrocytes were positive for OTR, we employed IHC-based three-dimensional
145 reconstruction using Imaris technique and combining immunohistochemical staining for GS
146 and GFAP with FISH for OTR mRNA in the rat CeL. Employing glial morphometric profiler,
147 we performed three-dimensional reconstruction of cells through a semi-automated pipeline²¹
148 (Fig. 1d-e). This analysis confirmed the presence of OTR mRNA in astrocytes and revealed
149 that OTR+ astrocytes have on average a significantly larger cell volume, surface area, a
150 higher number and an increased length of processes compared to OTR- astrocytes (Fig.
151 1e). Subsequent Sholl analysis revealed that OTR+ astrocytes bear more complex
152 morphological features than OTR- astrocytes (Fig. 1f), suggesting that OTR+ astrocytes
153 represent a distinct subpopulation of astrocytes within the CeL.

154

155 To test whether CeL astrocytes respond to endogenous OT release, we expressed the
156 ChR1/VChR1 chimaera channel rhodopsin variant²² (referred here as C1V1) in OTergic
157 neurons to optogenetically control CeA-innervating OT axons (Pot-C1V1-mCherry; referred
158 to as OxytOpto). To this end, we employed a previously characterized adeno-associated viral
159 vector (AAV) equipped with the OT promoter⁴, which was injected into the paraventricular
160 (PVN), supraoptic, and accessory nuclei of rat hypothalamus (Fig. 2a). First, we validated
161 that red shifted light ($\lambda 542$ nm light pulses of 10 ms width at 30 Hz) induced activation of
162 C1V1-expressing OT neurons in the PVN (Extended Data Fig. 2a-b). We then identified CeL
163 astrocytes through sulforhodamine 101 (SR101) labeling in acute brain slices and confirmed
164 astrocytes specificity of the labeling by measuring electrophysiological properties of SR101-
165 labelled cells in CeL (Extended Data Fig. 2c-e). We then assessed SR101 labeled astrocytes
166 activity by measuring the relative changes in cytosolic calcium using the small organic dye
167 Oregon Green[®] 488 BAPTA-1 (OGB1). (Fig. 2b). We found that of recorded astrocytes,
168 $61.9\pm 8.7\%$ responded to the optogenetic OT axons stimulation (Fig. 2c-d). To avoid the
169 possibility that astrocyte activity was increased due to the increased spiking of CeL
170 interneurons caused by optogenetically evoked OT release, tetrodotoxin (TTX) was added to
171 the bath prior the stimulation. Further calcium imaging experiments described below use
172 TTX incubation (if not stated otherwise) for the same reason,. We also compared the
173 frequency of calcium transients as well as the area under the curve before and after
174 optogenetic stimulation, expressing the results as a ratio between post-stimulation and
175 baseline values (referred to as AUC and Ca^{2+} transient frequency normalized to baseline,

176 analysis method detailed in Extended Data Fig. 2f). As depicted in Fig. 2d, both parameters
177 were increased following stimulation of OT axons. Taken together, these results indicate that
178 optogenetically-evoked OT release from axons present in the CeL elicits an increase in
179 activity of CeL astrocytes.

180

181 To ensure that the observed responses are exclusively due to OTR activation, we applied the
182 selective agonist of OTR ([Thr⁴Gly⁷]-oxytocin, TGOT), which increased calcium transients in
183 60.1±9.2% of the recorded astrocytes, a result unchanged when replicated with slices pre-
184 incubated with TTX (Fig. 2e-f). Similar pre-incubation of the slices with the OTR antagonist
185 [d(CH₂)⁵,Tyr(Me)²,Orn⁸]-vasotocin (dOVT) reduced the proportion of TGOT-evoked calcium
186 responses in astrocytes and their properties (Fig. 2e-f), confirming that the activation of
187 astrocytes by TGOT is indeed mediated by OTR. However, it cannot be discarded that other
188 OTR-mediated and astrocyte-independent mechanisms may drive CeL astrocyte activity up.

189

190 To exclude this possibility, we employed a transgenic mouse line with a LoxP sites flanking
191 the OTR gene²³ (OTR cKO mice). To specifically delete OTRs in astrocytes, we injected an
192 AAV driving expression of Cre recombinase under the control of the GFAP promoter in the
193 CeL (P_{GFAP}-Cre, Fig. 2g). This led to to expression of Cre in 56.0±4.9% of astrocytes within
194 the injection site, with a specificity reaching 96.2±2.1% (Extended Data Fig. 2g). P_{GFAP}-Cre
195 AAV injection in OTR cKO mice resulted in a drastic decrease in OTR mRNA signal in
196 astrocytes (Fig 2h), but not in neurons (Extended Data Fig. 2h). Similarly to results obtained
197 in rats, TGOT application in TTX-treated acute slices of the CeL from control mice led to
198 responses in 43.9±7.2% of astrocytes (Fig. 2i), whereas these responses were largely
199 reduced in CeL astrocytes from P_{GFAP}-Cre AAV injected OTR cKO mice (GFAP OTR KO,
200 Fig. 2i). These results confirm that astrocytes respond directly to OTR activation
201 independently from TGOT effects on CeL neurons.

202

203 **Activation of OTR+ astrocytes propagates through an astrocyte network**

204

205 Since astrocytes are known to form extensive intercellular networks, we next studied the
206 spatial connectivity of OTR+ astrocytes in the CeL. (Fig. 3a, Extended Data Fig. 3a). We
207 found that the distance between OTR+ astrocyte pairs (95.8±4.0µm) was larger than the
208 distance between OTR- astrocyte pairs (37.4±0.9µm, Fig. 3a). In addition, we found that
209 OTR+ astrocytes had significantly more contacts with OTR-, than with OTR+ astrocytes (Fig.
210 3a), whereas OTR- regularly contact other OTR- astrocytes (3.7±1.3 contacts).

211

212 These anatomical results suggest a specific distribution pattern of OTR+ astrocytes within
213 the CeL, where OTR+ astrocytes are found distant from their counterparts and exhibit
214 numerous connections with others, OTR- astrocytes. Interestingly, the proportion of rats and
215 mice astrocytes responsive to OTR activation always exceeded 40% of recorded cells (Fig.
216 2) despite our FISH/Imaris results indicating that less than 20% of astrocytes expressed
217 OTRs mRNA (Fig. 1). This apparent discrepancy led us to test whether the minor population
218 of OTR+ astrocytes could spread their activation following OTR signaling to a much larger
219 population of OTR- astrocytes.

220

221 There are two common signaling pathways typical for astrocytes which could facilitate the
222 spread of activation from OTR+ to OTR- astrocytes: (i) paracrine purinergic communication
223 and (ii) gap-junctions mediated spread of activity. To decipher the underlying mechanism, we

224 first blocked purinergic receptors using pyridoxalphosphate-6-azophenyl-2',4'-disulfonic acid
225 (PPADS) and found that this blocker did not significantly affect the average proportion of
226 astrocytes activated by TGOT (Fig. 3b), nor the properties of these responses (Fig. 3b), a
227 result replicated using a set of purinergic receptors antagonists blocking the majority of
228 known purinergic receptors (Extended Data Fig. 3b-c). Yet, the incubation with the gap-
229 junctions blocker carbenoxolone (CBX) significantly reduced the number of astrocytes
230 responsive to TGOT+TTX application (Fig. 3b). Given that astrocyte gap-junctions are
231 primarily composed of the connexins (Cx) 30 and 43, we further tested their involvement in
232 OTR-induced signal spreading by using a Cx30/Cx43 double KO mice line, previously shown
233 to lack astrocyte gap junctional communication²⁴ (Fig. 3c). As found with CBX, the number of
234 astrocytes activated by TGOT was significantly reduced in these mice (Fig. 3c). These
235 results indicate that gap junctions play a role in the propagation of responses following OTR
236 activation in the CeL astrocytes network, possibly from OTR+ to OTR- astrocytes. This is
237 corroborated by the anatomical observations that biocytin infused in the cytosol of astrocytes
238 spread from one cell to another within the CeL network at least in part via gap-junctions (Fig.
239 4e).

240
241

242 **CeL astrocyte activity increases CeL neurons excitability**

243

244 We next wanted to test if this direct astrocyte network response to OTR activation could be
245 relevant to the known effect of OTR signaling on CeA neuronal networks^{4,13,14}. To
246 manipulate astrocytic activity, we expressed the opsin C1V1 under the control of the GFAP
247 promoter using rAAV injections (PGFAP-C1V1-mCherry; referred to as AstrOpto, Fig. 4a).
248 After confirmation of vector expression in $62.5 \pm 3.1\%$ of all astrocytes in the CeL, with a
249 specificity reaching $98.8 \pm 0.7\%$ (Extended Data Fig. 4a), we evaluated the effect of C1V1
250 stimulation on astrocyte calcium activity (Fig. 4b). We observed responses in $60.8 \pm 9.0\%$ of
251 astrocytes (Fig. 4c), a proportion comparable to what we observed following OTR stimulation
252 by TGOT+TTX (AstrOpto vs TGOT+TTX: $p = 0.8265$, unpaired t -test). The removal of
253 extracellular calcium prevented the C1V1-driven astrocyte activity (Extended Data Fig. 4b).
254 This indicates that influx of extracellular calcium through the plasma membrane is required to
255 generate calcium transient activity in astrocytes following C1V1 activation (Extended Data
256 Fig. 4b).

257

258 Next, we measured the effect of evoked astrocyte activity, using AstrOpto or direct OTR
259 stimulation through TGOT application, on CeL neurons excitability measured through patch-
260 clamp techniques. Optical stimulation of C1V1 in astrocytes increased the frequency of
261 miniature excitatory post-synaptic currents (mEPSCs) in CeL neurons (Fig. 4d) while bath-
262 applied TGOT had a similar effect (Fig. 4f). We next infused BAPTA specifically in the
263 astrocyte network (Fig. 4e) to block the increase in calcium transients evoked by TGOT, and
264 found it also blocked TGOT effect on CeL neurons mEPSCs (Fig. 4e-f). This indicates that
265 OTR activation and the ensuing increased in calcium transients in astrocytes is driving up
266 excitatory inputs to CeL neurons.

267

268 To identify the intercellular communication pathway involved in astrocytes-neurons
269 communication following OTR-dependent activation of astrocytes, we studied whether N-
270 Methyl-D-Aspartate receptor (NMDAR), a well-known neuronal receptor that can be activated

271 by astrocytic gliotransmission^{12,25,26}, was involved. Thus, we applied a NMDAR antagonist
272 (2R)-amino-5-phosphonovaleric acid (AP5) prior to TGOT application and found it inhibited
273 TGOT effect on mEPSCs frequency (Fig. 4f). Importantly, AP5 had no effect on astrocyte
274 responses to TGOT, thereby excluding the involvement of NMDAR in CeL astrocytes
275 responses to TGOT (Extended Data Fig. 3d). Finally, to unambiguously demonstrate that
276 astrocytes underlie the effect of OTR signaling on CeL neuron excitatory synaptic
277 transmission, we repeated the mEPSCs measurements in control and GFAP OTR KO mice.
278 TGOT application increased mEPSCs frequency in control mice, but not in GFAP OTR KO
279 mice (Fig. 4g-h), confirming the role of astrocytic OTR in mediating the effects of OTR
280 signaling on synaptic inputs in CeL neurons.

281

282 We then investigated whether the increase in mEPSCs frequency in CeL neurons following
283 OTR activation was able to increase their firing frequency. To address this question, we
284 applied the same stimulation protocols as before, and subsequently recorded spontaneous
285 action potential (AP) firing (Fig. 5a-b). First, AstrOpto increased firing of CeL neurons, an
286 effect that was blocked by previous infusion of BAPTA in the astroglial network, hence
287 proving its dependence on astrocyte calcium signaling (Fig. 5c). Similarly, and in agreement
288 with its effect on CeL neurons mEPSC, TGOT also increased neuronal spiking activity (Fig.
289 5d), an effect which was abolished following either BAPTA infusion in the astroglial network
290 or pre-incubation of AP5 in the recording bath (Fig. 5d). Crucially, TGOT application
291 increased the firing of CeL neurons in control but not in GFAP OTR KO mice (Fig. 5e-f).

292

293 These results unequivocally demonstrate that OTR signaling in the CeL requires the
294 expression and activation of OTR and its associated calcium signaling in astrocytes, which
295 further lead to an increase in the excitability of CeL interneurons through NMDAR-dependent
296 mechanisms.

297

298 **CeL astrocytes activity increases inhibitory inputs onto CeM projection neurons**

299

300 Previous work showed that the activation of CeL OTRs leads to an increased activity of
301 GABAergic CeL neurons, a result we replicated here (Fig. 5). A demonstrated direct
302 consequence of this is an increased frequency of GABA_A-mediated inhibitory post-synaptic
303 currents (IPSCs) in CeM projection neurons^{4,13,14}.

304

305 In agreement with these findings, we found that optogenetic activation of CeL astrocytes
306 (through AstrOpto) evoked an increase in IPSC frequency in rat CeM neurons (Fig. 6a-c).
307 This effect was also dependent on CeL astrocytic calcium signaling, as BAPTA infusion in
308 CeL astrocytes abolished it (Fig. 6c). Furthermore, the effect of AstrOpto on CeM IPSCs
309 frequency was suppressed by application of AP5, but also by prior degradation of D-serine
310 (an NMDAR co-agonist) with D-amino acid oxidase (DAAO) (Extended Data Fig. 5a). D-
311 Serine is a known gliotransmitters, whose levels have been found to be increased following
312 astrocytic GPCR activation²⁷. Altogether, these results indicate that the effect of AstrOpto on
313 IPSCs in CeM neurons is dependent on the activation of NMDARs in CeL neurons. TGOT
314 application produced a similar effect on CeM neurons, also dependent on CeL astrocytic
315 calcium signaling (Fig. 6d) and on NMDARs (Fig. 6d). Initial incubation with DAAO similarly
316 blocked the effect of TGOT on IPSCs frequency (Extended Data Fig. 5b). Crucially, D-serine
317 supplementation in the DAAO-treated slices following the first, effectless, TGOT application
318 rescued the effect of a second TGOT application on IPSCs frequency (Extended Data Fig.

319 5b-d). This confirms the involvement of neuronal NMDARs and its co-agonist D-Serine in
320 OTR-mediated modulation of CeA neuronal network. To further complement these results,
321 we found that bath application of 5,7-dichlorokynurenic acid (DCKA), a potent antagonist of
322 the NMDAR glycine/D-Serine modulatory site, also abolished TGOT effects on CeM IPSC
323 frequency, while the AMPAR antagonist DNQX had no effect (Extended Data Fig. 5e). In
324 addition, pre-incubation with the purinergic receptors antagonists PPADS, CPT or SCH
325 58261 had no effects either (Extended Data Fig. 5f). This confirms that the primary mode of
326 astrocyte to neuron communication engaged following OTR signaling in CeA involves
327 NMDARs, but not purinergic signaling in neurons, and is mediated by an increase in D-serine
328 levels.

329

330 As in rats, TGOT application also led to an increased IPSC frequency in CeM neurons in
331 brain slices from control mice, but not in slices from GFAP OTR KO mice (Fig. 6e-f). These
332 *ex vivo* results clearly demonstrate that direct of OTR-mediated CeL astrocytes activation
333 leads to an NMDAR-dependent increase in CeL neurons excitability, which further increases
334 inhibitory inputs into CeM projection neurons.

335

336 Our data so far demonstrate that when OTR signaling is engaged in astrocytes, these cells
337 increase the excitability of CeL neurons, directly leading to an increase in inhibitory inputs
338 into CeM projection neurons. Altogether, these results demonstrate that the effect of OT
339 neuronal activity is abolished when astrocyte function is compromised, establishing for the
340 first time that OT signaling in CeA circuitry is locally transduced by astrocytes.

341

342 **OTR signaling through astrocytes is crucial for emotional balance regulation.**

343

344 The CeA is a key nucleus for the processing of emotional information, and notably plays an
345 important role in pain-associated disorders¹⁶, for which OT has been demonstrated as a
346 crucial regulator¹⁹. We therefore chose to first test the involvement of OTR-mediated (or
347 direct) astrocyte activation in modulating mechanical pain hypersensitivity (Fig. 7b,f), levels
348 of anxiety (Fig. 7c,g), and reinforcement behavior (Fig. 7f,h) in rats and mice that developed
349 neuropathic pain and the associated increased anxiety following a spared nerve injury (SNI)
350 surgery²⁸ (Extended Data Fig. 6a).

351

352 Given that there is a proven link between chronic pain etiology and synaptic changes in the
353 CeA²⁹, we initially tested whether the effect of TGOT on astrocytes calcium signaling and
354 CeM neurons IPSCs frequency was altered in SNI rats, but did not find any differences
355 compared to sham-operated animals (Extended Data Fig. 6b-c). This indicates that OTR
356 signaling in CeA, at least at the levels of the circuit studied here, is unaltered in SNI animals.
357 We further confirmed that D-Serine was still required for TGOT effects in the CeA of SNI
358 animals using DAAO pre-incubation followed by exogenous D-Serine supplementation in the
359 *ex vivo* setting (Extended Data Fig. 6d).

360

361 Following our finding that SNI procedure did not alter the effect of TGOT at the circuit level,
362 we next used a nociceptive assay to measure the mechanical threshold for paw withdrawal in
363 both rats and mice. We found that SNI animals displayed a decreased mechanical threshold,
364 but bilateral micro-injections of TGOT in the CeA had no clear effect on it, with only a mild
365 anti-nociceptive effect only in rats (Fig. 7b,f). Moreover, bilateral optogenetic stimulation of

366 rats CeL astrocytes (AstrOpto) had no noticeable effect on mechanical threshold in rats (Fig.
367 7b; Extended Data Fig. 7b).

368

369 Next we performed an elevated plus maze (EPM) test, and found that SNI animals spent
370 significantly more time in the closed arm compared to sham-operated ones, indicating the
371 SNI procedure induced a state of elevated anxiety (Fig. 7c,g) as expected. When TGOT was
372 injected in CeA, time spent in the closed arm was significantly reduced to levels comparable
373 to those observed in sham animals, indicating an anxiolytic effect of OTR signaling in both
374 rats and mice (Fig. 7c,g). Crucially, AstrOpto in rats had a comparable effect (Fig. 7c), while
375 the deletion of OTR from CeL astrocytes in mice abolished the anxiolytic effects of TGOT
376 (Fig. 7g), highlighting the involvement of astrocytic OTRs also at the behavioral level.
377 Interestingly, sham mice with deletion of OTR in CeL astrocytes displayed an anxious
378 behavior (Fig. 7g), which indicates OTR signaling through astrocytes is involved in emotional
379 balance, even under pain-free conditions.

380

381 In order to further investigate the role of the CeA in attributing emotional valence to stimuli,
382 we used the conditioned place preference (CPP) test in rats and mice that underwent an SNI
383 or sham procedures. Here, both SNI and sham animals exhibited a clear preference for the
384 chamber paired with TGOT infusion (Fig. 7d,h). The optogenetic activation of astrocytes in
385 rat CeL also led to a place preference, mimicking TGOT action (Fig. 7d), while TGOT lost its
386 positive conditioning effects in GFAP OTR KO mice (Fig. 7h). Importantly, neither the
387 treatments nor the SNI procedure significantly affected the motor activity of rats and mice in
388 both the EPM or CPP tests (Extended Data Fig. 7).

389

390 Collectively, our findings demonstrate from the local circuit to the behavioral levels that OTR
391 signaling through CeL astrocytes is a novel and important mechanism involved in emotional
392 states regulation, this under both normal and chronic pain conditions (Fig. 7i).

393

394
395
396

DISCUSSION

397 We here demonstrate that OTR signaling through astrocytes is crucial for the oxytocinergic
398 modulation of the local CeA microcircuit and its behavioral correlates. We further propose
399 that this effect relies on a morphologically defined subpopulation of OTR+ astrocytes (Fig. 1-
400 2), that convey their activation by OT to other astrocytes through gap-junctional
401 communication (Fig. 3), leading to an increase in activity in the majority of CeL astrocytes
402 (Fig. 2-3). In turn, astrocytes increase the excitability of CeL interneurons by gating activation
403 of NMDA receptors (Fig. 4-5), leading to an increase in GABAergic inhibitory inputs in post-
404 synaptic neurons located in the CeM (Fig. 6). At the behavioral level, this OTR-mediated
405 modulation of CeA astro-neuronal network promotes a positive emotional state, measured as
406 clear anxiolytic and positive reinforcement effects (Fig. 7).

407 Mechanistically, our results reinforce previous demonstrations of a role of astrocytes in
408 transforming neuromodulators signaling into a change in the gain of neuronal circuits, notably
409 by (co-)activating neuronal NMDAR^{12,25,26}. Despite the high proportion of OTR+ neurons (up
410 to 70%) compared to the limited number of OTR+ astrocytes (~18%) in the CeL, the
411 activation of OTRs in astrocytes was required to gate CeL neurons responses to OTR
412 activation by allowing a sustained (co)activation of NMDARs. Other mechanisms are
413 probably at play: OTR activation in CeL neurons might inhibit K+ leak current, as has been
414 shown in olfactory neuronal cells³⁰ and in spinal cord³¹. These mechanisms might act in
415 synergy to induce an elevation in firing rates of CeL neurons by increasing the gain of
416 excitatory inputs in these cells. Furthermore, similar mechanisms of astrocytes to neuron
417 communication through neuronal NMDARs (co)activation have been proposed by other
418 studies to favor a synchronous increase in excitability across an ensemble of neurons^{32,33}.
419 This would allow a synchronized and long-lasting switch in the gain of the CeA neuronal
420 circuits, thereby amplifying the effect of OT on CeA outputs in both the spatial and temporal
421 domains. In light of the predominantly non-synaptic mode of OT release from axons *en*
422 *passant*, which could lead to CeL-restricted micro-volume transmission of the neuropeptide⁵,
423 it seems then plausible that astrocytes are required to relay and amplify OT signaling to CeL
424 neurons. Another mechanism that was repeatedly found to be involved in neuromodulators
425 signaling through astrocytes is the activation of purinergic signaling in neurons^{34,35}. However,
426 in the case of OT signaling within the CeA, purinergic signaling was not involved (Extended
427 Data Fig. 5). It would then be interesting to test if astrocytes are important to OT signaling in
428 other brain regions, and if they are, if the same mechanisms of astrocytes to neurons
429 communication are at stake.

430 We found that CeA astrocytes can be divided into two defined populations: OTR+ and OTR-
431 astrocytes. OTR+ astrocytes are morphologically more complex and have more close
432 contacts with neighboring, OTR- astrocytes, while being quite distant from their OTR+
433 counterparts with whom they have almost no contacts (Fig. 1, 2). Thus, we hypothesize that
434 these morphological peculiarities allow the propagation of OTR evoked calcium transients
435 (Fig. 2) to a much larger number of OTR- astrocytes through, at least partially, gap junctions
436 (Fig. 3b-c). Therefore only a few, strategically positioned OTR+ astrocytes are sufficient to
437 result in a network wide effect of OT release in the CeL, despite the relatively moderate
438 number of OT fibers found in this nucleus⁴. By describing a new population of astrocytes, our

439 work add to the recent advances in describing molecular, morphological and functional
440 heterogeneity in astrocytes population^{36,37} and opens up new perspectives into
441 understanding how astrocytes subpopulations are functionally organized and communicate
442 inside CNS circuits.

443 OT and its effects on brain circuits, and ultimately behavior, are under intense scrutiny, from
444 fundamental research in animal models to behavioral and physiological studies in
445 humans^{38,39}. Among other roles, OT is considered a powerful anxiolytic peptide through its
446 action in the human amygdala⁴⁰. Yet, all studies so far considered as an accomplished fact
447 that OT was acting directly on neurons, despite the controversies regarding the cellular
448 substrates of BOLD fMRI signals often used in human studies, with some results arguing for
449 a major contribution of astrocyte activity to these signals^{41,42}. Furthermore, a significant
450 number of studies demonstrated that astrocytes or their invertebrates counterparts are key, if
451 not primary, targets of neuromodulators^{12,25,26,34,35,43}, and that astrocytes might be the causal
452 elements behind shifts in brain states^{11,43,44}, a function usually attributed mainly to
453 neuromodulators direct action on neurons⁴⁵. Thus, further research focused on astrocytes-
454 mediated modulation of human brain circuits' activities is particularly promising to develop
455 refined strategies for future therapeutic approaches. Indeed, neuromodulators are the targets
456 of numerous, already available, treatments of psychiatric diseases using either small
457 molecule drugs or electrical stimulation protocols, such as deep brain⁴⁶ or transcranial
458 stimulations⁴⁷, for which astrocytes also seem particularly involved^{46,47}. Taken together, this
459 indicates a need for a more global and systematic consideration of astrocytes roles in brain
460 circuits, notably regarding the effect of neuromodulators, and in particular OT. We believe
461 this is especially relevant for the development of better therapeutics in the field of chronic
462 pain, which imposes a massive burden to society, impacting ~20% of the global population⁴⁸.

463 Indeed, considering that general anxiety and depression are frequent comorbidity of chronic
464 pain⁴⁹, our finding that the activation of OT signaling in CeL astrocytes promotes a form of
465 emotional comfort by alleviating anxious behavior and has positive reinforcement properties
466 is promising: it demonstrates that activation of a particular, astrocyte-mediated, OTR
467 pathways affect one of the most impactful aspect of the chronic pain sphere, the emotional
468 one. This further highlights astrocytes as important cellular substrates of emotional
469 regulation, which several studies have also argued for (see⁵⁰ and references therein). In this
470 context, targeting the OT system and/or astrocytes specifically, in the amygdala or other
471 CNS regions, might lead to the development of new therapeutic avenues to improve patient's
472 well-being.

473
474
475

476
477
478
479
480
481
482
483
484
485
486
487
488
489
490
491
492
493
494
495
496
497
498
499
500
501
502
503
504

ACKNOWLEDGEMENTS

This work was supported by the IASP Early Career Research grant 2012, FP7 Career Integration grant 334455, Initiative of Excellence (IDEX) Attractiveness grant 2013, IDEX Interdisciplinary grant 2015, University of Strasbourg Institute for Advanced Study (USIAS) fellowship 2014-15, Foundation Fyssen research grant 2015, NARSAD Young Investigator Grant 24821, ANR JCJC grant (to AC); ANR-DFG grant GR 3619/701 (to AC and VG); Alexander von Humboldt fellowship (to DH), Seed grant from DFG within the Collaborative center SFB 1158 and Fyssen Foundation fellowship (to AL), DFG grants GR 3619/13-1 and GR 3619/16-1 (to VG), SFB 1158 (to CP, JS, and VG); SNSF-DFG grant GR 3619/8-1 (to RS and VG), Fritz Thyssen foundation (to VG); DFG Postdoc Fellowship AL 2466/1-1 to FA, Alexander von Humboldt Foundation (to DH); Fyssen foundation and PROCOP grant and SFB1158 seed grant for young scientists (to AL); Research Foundation - Flanders, fellowship (12V7519N) (to JW); Russian Science Foundation RSF (17-75-10061) and the Subsidy Allocated to the Kazan Federal University for the State Assignment № 0671-2020-0059 (to AR); the intramural research program of the NIMH (ZIAMH002498) (to WSY); National Institutes of Health grants R01NS094640 and R01HL090948 (to JES). European Research Council (Consolidator grant #683154) and European Union's Horizon 2020 research and innovation program (Marie Sklodowska-Curie Innovative Training Networks, grant #722053, EU-GliaPhD) (to NR). The authors thank Vincent Lelièvre for *in situ* hybridization advices; Romain Goutagny for *in vivo* optogenetics assistance; Fulvio Magara for anxiety behavior advices; Barbara Kurpiers and the Interdisciplinary Neurobehavioral Core Facility of Heidelberg University for experiments performed there; Sophie Reibel and the Chronobiotron UMS 3415 for all animal care; Thomas Splettstoesser (www.scistyle.com) for the help with the preparation of figure 7.

505

506 **AUTHOR CONTRIBUTIONS**

507

508 Conceptualization, AC; Methodology, AC, BBo, CML, CP, DK, FA, ID, JES, JW, JYC, NR,
509 PD, PP, RS, VG, WSY, YG; Analysis, AC, BBe, BBJ, CML, DK, FA, HSKB, JW, SG; *In situ*
510 hybridization, DH, FA, HSKB, HW, JS, ME; Immunohistochemistry, AL, DH, FA, JW, ME,
511 MdSG; Imaris analysis: FA, MKK, RKR; *Ex vivo* patch-clamp electrophysiology, AB, AC, JW,
512 SG, DK, IW, BBe, MA; *Ex vivo* calcium imaging, AB, CML, DK, JW; Astrocytes
513 characterization, AB, AR, BBe, DK, IW, ME, SG; Behavior, AC, BBJ, DK, JW; Mice line
514 validation, WSY; Viral vectors validation, MdSG, ME, VG; Spared nerve injuries, PI, MP;
515 Writing, AB, AC, DK, FA, JW, VG; Funding acquisition AC, VG; Supervision, AC, VG; Project
516 administration, AC.

517

518

519 **DECLARATION OF INTERESTS**

520

521 The authors declare no competing interest

522

523 REFERENCES

524

- 525 1. Lee, H.-J., Macbeth, A. H., Pagani, J. H. & Young, W. S. Oxytocin: the great facilitator
526 of life. *Prog. Neurobiol.* **88**, 127–51 (2009).
- 527 2. Gimpl, G. & Fahrenholz, F. The oxytocin receptor system: structure, function, and
528 regulation. *Physiol. Rev.* **81**, 629–83 (2001).
- 529 3. Theodosis, D. T. Oxytocin-secreting neurons: A physiological model of morphological
530 neuronal and glial plasticity in the adult hypothalamus. *Front. Neuroendocrinol.* **23**,
531 101–35 (2002).
- 532 4. Knobloch, H. S. *et al.* Evoked axonal oxytocin release in the central amygdala
533 attenuates fear response. *Neuron* **73**, 553–66 (2012).
- 534 5. Chini, B., Verhage, M. & Grinevich, V. The Action Radius of Oxytocin Release in the
535 Mammalian CNS: From Single Vesicles to Behavior. *Trends Pharmacol. Sci.* **38**, 982–
536 991 (2017).
- 537 6. Kuo, J., Hariri, O. R. & Micevych, P. An interaction of oxytocin receptors with
538 metabotropic glutamate receptors in hypothalamic astrocytes. *J. Neuroendocrinol.* **21**,
539 1001–6 (2009).
- 540 7. Wang, P., Qin, D. & Wang, Y.-F. Oxytocin Rapidly Changes Astrocytic GFAP Plasticity
541 by Differentially Modulating the Expressions of pERK 1/2 and Protein Kinase A. *Front.*
542 *Mol. Neurosci.* **10**, 1–14 (2017).
- 543 8. Mitre, M. *et al.* A Distributed Network for Social Cognition Enriched for Oxytocin
544 Receptors. *J. Neurosci.* **36**, 2517–2535 (2016).
- 545 9. Yoshida, M. *et al.* Evidence that oxytocin exerts anxiolytic effects via oxytocin receptor
546 expressed in serotonergic neurons in mice. *J. Neurosci.* **29**, 2259–71 (2009).
- 547 10. Hirase, H., Iwai, Y., Takata, N., Shinohara, Y. & Mishima, T. Volume transmission
548 signalling via astrocytes. *Philos. Trans. R. Soc. B Biol. Sci.* **369**, 20130604–20130604
549 (2014).
- 550 11. Kjaerby, C., Rasmussen, R., Andersen, M. & Nedergaard, M. Does Global Astrocytic
551 Calcium Signaling Participate in Awake Brain State Transitions and Neuronal Circuit
552 Function? *Neurochem. Res.* **42**, 1810–1822 (2017).
- 553 12. Papouin, T., Dunphy, J. M., Tolman, M., Dineley, K. T. & Haydon, P. G. Septal
554 Cholinergic Neuromodulation Tunes the Astrocyte-Dependent Gating of Hippocampal
555 NMDA Receptors to Wakefulness. *Neuron* **94**, 840-854.e7 (2017).
- 556 13. Huber, D., Veinante, P. & Stoop, R. Vasopressin and oxytocin excite distinct neuronal
557 populations in the central amygdala. *Science* **308**, 245–8 (2005).
- 558 14. Viviani, D. *et al.* Oxytocin selectively gates fear responses through distinct outputs
559 from the central amygdala. *Science* **333**, 104–7 (2011).
- 560 15. Han, R. T. *et al.* Long-Term Isolation Elicits Depression and Anxiety-Related
561 Behaviors by Reducing Oxytocin-Induced GABAergic Transmission in Central
562 Amygdala. *Front. Mol. Neurosci.* **11**, 246 (2018).
- 563 16. Neugebauer, V., Li, W., Bird, G. C. & Han, J. S. The amygdala and persistent pain.
564 *Neuroscientist* **10**, 221–234 (2004).
- 565 17. Tye, K. M. *et al.* Amygdala circuitry mediating reversible and bidirectional control of
566 anxiety. *Nature* **471**, 358–62 (2011).
- 567 18. Ji, R.-R., Donnelly, C. R. & Nedergaard, M. Astrocytes in chronic pain and itch. *Nat.*
568 *Rev. Neurosci.* **20**, 667–685 (2019).
- 569 19. Poisbeau, P., Grinevich, V. & Charlet, A. Oxytocin Signaling in Pain: Cellular, Circuit,
570 System, and Behavioral Levels. *Curr. Top. Behav. Neurosci.* (2017).
571 doi:10.1007/7854_2017_14
- 572 20. Martin-Fernandez, M. *et al.* Synapse-specific astrocyte gating of amygdala-related
573 behavior. *Nat. Neurosci.* **20**, 1540–1548 (2017).
- 574 21. Althammer, F. *et al.* Three-dimensional morphometric analysis reveals time-dependent
575 structural changes in microglia and astrocytes in the central amygdala and
576 hypothalamic paraventricular nucleus of heart failure rats. *J. Neuroinflammation* **17**,

- 577 221 (2020).
- 578 22. Yizhar, O. *et al.* Neocortical excitation/inhibition balance in information processing and
579 social dysfunction. *Nature* **477**, 171–178 (2011).
- 580 23. Lee, H. J., Caldwell, H. K., Macbeth, A. H., Tolu, S. G. & Young, W. S. A conditional
581 knockout mouse line of the oxytocin receptor. *Endocrinology* **149**, 3256–3263 (2008).
- 582 24. Wallraff, A. *et al.* The impact of astrocytic gap junctional coupling on potassium
583 buffering in the hippocampus. *J. Neurosci.* **26**, 5438–47 (2006).
- 584 25. Robin, L. M. *et al.* Astroglial CB1 Receptors Determine Synaptic D-Serine Availability
585 to Enable Recognition Memory. *Neuron* **98**, 935–944.e5 (2018).
- 586 26. Corkrum, M., Rothwell, P. E., Thomas, M. J., Kofuji, P. & Araque, A. Opioid-Mediated
587 Astrocyte-Neuron Signaling in the Nucleus Accumbens. *Cells* **8**, 586 (2019).
- 588 27. Robin, L. M. *et al.* Astroglial CB1 Receptors Determine Synaptic D-Serine Availability
589 to Enable Recognition Memory. *Neuron* **0**, 1–10 (2018).
- 590 28. Decosterd, I. & Woolf, C. J. Spared nerve injury: an animal model of persistent
591 peripheral neuropathic pain. *Pain* **87**, 149–158 (2000).
- 592 29. Thompson, J. M. & Neugebauer, V. Amygdala Plasticity and Pain. *Pain Res. Manag.*
593 **2017**, 8296501 (2017).
- 594 30. Gravati, M. *et al.* Dual modulation of inward rectifier potassium currents in olfactory
595 neuronal cells by promiscuous G protein coupling of the oxytocin receptor. *J.*
596 *Neurochem.* **114**, 1424–1435 (2010).
- 597 31. Breton, J.-D. *et al.* Oxytocin-induced antinociception in the spinal cord is mediated by
598 a subpopulation of glutamatergic neurons in lamina I-II which amplify GABAergic
599 inhibition. *Mol. Pain* **4**, 19 (2008).
- 600 32. Angulo, M. C., Kozlov, A. S., Charpak, S. & Audinat, E. Glutamate released from glial
601 cells synchronizes neuronal activity in the hippocampus. *J. Neurosci.* **24**, 6920–6927
602 (2004).
- 603 33. Fellin, T. *et al.* Neuronal synchrony mediated by astrocytic glutamate through
604 activation of extrasynaptic NMDA receptors. *Neuron* **43**, 729–43 (2004).
- 605 34. Corkrum, M. *et al.* Dopamine-Evoked Synaptic Regulation in the Nucleus Accumbens
606 Requires Astrocyte Activity. *Neuron* **105**, 1036–1047.e5 (2020).
- 607 35. Ma, Z., Stork, T., Bergles, D. E. & Freeman, M. R. Neuromodulators signal through
608 astrocytes to alter neural circuit activity and behaviour. *Nature* **539**, 428–432 (2016).
- 609 36. Pestana, F., Edwards-Faret, G., Belgard, T. G., Martirosyan, A. & Holt, M. G. No
610 longer underappreciated: The emerging concept of astrocyte heterogeneity in
611 neuroscience. *Brain Sci.* **10**, 1–21 (2020).
- 612 37. Khakh, B. S. & Deneen, B. The Emerging Nature of Astrocyte Diversity. *Annu. Rev.*
613 *Neurosci.* **42**, 187–207 (2019).
- 614 38. Grinevich, V. & Neumann, I. D. Brain oxytocin: how puzzle stones from animal studies
615 translate into psychiatry. *Mol. Psychiatry* (2020). doi:10.1038/s41380-020-0802-9
- 616 39. Quintana, D. S. *et al.* Advances in the field of intranasal oxytocin research: lessons
617 learned and future directions for clinical research. *Mol. Psychiatry* (2020).
618 doi:10.1038/s41380-020-00864-7
- 619 40. Neumann, I. D. & Slattery, D. A. Oxytocin in General Anxiety and Social Fear: A
620 Translational Approach. *Biol. Psychiatry* **79**, 213–221 (2016).
- 621 41. Takata, N. *et al.* Optogenetic astrocyte activation evokes BOLD fMRI response with
622 oxygen consumption without neuronal activity modulation. *Glia* **66**, (2018).
- 623 42. Figley, C. R. & Stroman, P. W. The role(s) of astrocytes and astrocyte activity in
624 neurometabolism, neurovascular coupling, and the production of functional
625 neuroimaging signals. *Eur. J. Neurosci.* **33**, 577–588 (2011).
- 626 43. Kastanenka, K. V. *et al.* A roadmap to integrate astrocytes into Systems
627 Neuroscience. *GLIA* (2019). doi:10.1002/glia.23632
- 628 44. Poskanzer, K. E. & Yuste, R. Astrocytes regulate cortical state switching in vivo. *Proc.*
629 *Natl. Acad. Sci. U. S. A.* **2016**, 1–10 (2016).
- 630 45. McCormick, D. A., Nestvogel, D. B. & He, B. J. Neuromodulation of Brain State and
631 Behavior. *Annu. Rev. Neurosci.* **43**, 391–415 (2020).

- 632 46. Fenoy, A. J., Goetz, L., Chabardès, S. & Xia, Y. Deep brain stimulation: Are astrocytes
633 a key driver behind the scene? *CNS Neurosci. Ther.* **20**, 191–201 (2014).
- 634 47. Monai, H. & Hirase, H. Astrocytes as a target of transcranial direct current stimulation
635 (tDCS) to treat depression. *Neurosci. Res.* **126**, 15–21 (2018).
- 636 48. Mills, S. E. E., Nicolson, K. P. & Smith, B. H. Chronic pain: a review of its
637 epidemiology and associated factors in population-based studies. *Br. J. Anaesth.* **123**,
638 e273–e283 (2019).
- 639 49. Woo, A. K. Depression and Anxiety in Pain. *Rev. pain* **4**, 8–12 (2010).
- 640 50. Oliveira, J. F., Sardinha, V. M., Guerra-Gomes, S., Araque, A. & Sousa, N. Do stars
641 govern our actions? Astrocyte involvement in rodent behavior. *Trends Neurosci.* **38**,
642 535–49 (2015).
- 643 51. Rouach, N., Koulakoff, A., Abudara, V., Willecke, K. & Giaume, C. Astroglial metabolic
644 networks sustain hippocampal synaptic transmission. *Science* **322**, 1551–5 (2008).
- 645 52. Pannasch, U. *et al.* Astroglial networks scale synaptic activity and plasticity. *Proc. Natl.*
646 *Acad. Sci. U. S. A.* **108**, 8467–72 (2011).
- 647 53. Theis, M. *et al.* Accelerated hippocampal spreading depression and enhanced
648 locomotory activity in mice with astrocyte-directed inactivation of connexin43. *J.*
649 *Neurosci.* **23**, 766–76 (2003).
- 650 54. Teubner, B. *et al.* Connexin30 (Gjb6)-deficiency causes severe hearing impairment
651 and lack of endocochlear potential. *Hum. Mol. Genet.* **12**, 13–21 (2003).
- 652 55. Shigetomi, E. *et al.* Imaging calcium microdomains within entire astrocyte territories
653 and endfeet with GCaMPs expressed using adeno-associated viruses. *J. Gen.*
654 *Physiol.* **141**, 633–647 (2013).
- 655 56. Ting, J. T. *et al.* Preparation of Acute Brain Slices Using an Optimized N-Methyl-D-
656 glucamine Protective Recovery Method. *J. Vis. Exp.* 1–13 (2018). doi:10.3791/53825
- 657 57. Serrano, A., Haddjeri, N., Lacaille, J., Robitaille, R. & Centre-ville, S. GABAergic
658 Network Activation of Glial Cells Underlies Hippocampal Heterosynaptic Depression.
659 *J. Neurosci.* **26**, 5370–5382 (2006).
- 660 58. Jourdain, P. *et al.* Glutamate exocytosis from astrocytes controls synaptic strength.
661 *Nat. Neurosci.* **10**, 331–9 (2007).
- 662 59. Ikegaya, Y., Le Bon-Jego, M. & Yuste, R. Large-scale imaging of cortical network
663 activity with calcium indicators. *Neurosci. Res.* **52**, 132–138 (2005).
- 664 60. Shigetomi, E., Bowser, D. N., Sofroniew, M. V & Khakh, B. S. Two forms of astrocyte
665 calcium excitability have distinct effects on NMDA receptor-mediated slow inward
666 currents in pyramidal neurons. *J. Neurosci.* **28**, 6659–63 (2008).
- 667 61. Anlauf, E. & Derouiche, A. Glutamine synthetase as an astrocytic marker: its cell type
668 and vesicle localization. *Front. Endocrinol. (Lausanne).* **4**, 144 (2013).
- 669 62. Luis-Delgado, O. E. *et al.* Calibrated forceps: A sensitive and reliable tool for pain and
670 analgesia studies. *J. Pain* **7**, 32–39 (2006).
- 671 63. Walf, A. A. & Frye, C. A. The use of the elevated plus maze as an assay of anxiety-
672 related behavior in rodents. *Nat. Protoc.* **2**, 322–8 (2007).
- 673 64. King, T. *et al.* Unmasking the tonic-aversive state in neuropathic pain. *Nat. Neurosci.*
674 **12**, 1364–1366 (2009).
- 675 65. Virtanen, P. *et al.* SciPy 1.0: fundamental algorithms for scientific computing in Python.
676 *Nat. Methods* **17**, 261–272 (2020).
- 677 66. Zeisel, A. *et al.* Cell types in the mouse cortex and hippocampus revealed by single-
678 cell RNA-seq. *Science (80-)*. **347**, 1138–1142 (2015).
- 679 67. Batiuk, M. Y. *et al.* Identification of region-specific astrocyte subtypes at single cell
680 resolution. *Nat Commun* **11**, 1220 (2020).
- 681 68. Kofuji, P. & Araque, A. G-Protein-Coupled Receptors in Astrocyte–Neuron
682 Communication. *Neuroscience* (2020). doi:10.1016/j.neuroscience.2020.03.025
- 683 69. Oceau, J. C. *et al.* Transient, Consequential Increases in Extracellular Potassium Ions
684 Accompany Channelrhodopsin2 Excitation. *Cell Rep.* **27**, 2249–2261.e7 (2019).
- 685 70. Reeves, A. M. B., Shigetomi, E. & Khakh, B. S. Bulk loading of calcium indicator dyes
686 to study astrocyte physiology: Key limitations and improvements using morphological

687
688

maps. *J. Neurosci.* **31**, 9353–9358 (2011).

689
690
691
692
693
694
695
696
697
698
699
700
701
702
703
704
705
706
707
708
709
710
711
712
713
714
715
716
717
718
719
720
721
722
723
724
725
726
727
728
729
730
731
732
733
734
735
736

FIGURE TITLES AND LEGENDS

Figure 1. Specific CeL astrocytes express oxytocin receptors. (a) Overview of CeA fluorescent *in situ* hybridization of OTR mRNA (red) and glutamine synthase immunostaining (GS, green). (b) High magnification images of cells positive for OTR mRNA and/or GS (double arrows); green arrows point GS positive cells; red arrows point OTR mRNA-positive cells. Scale bars are 100 (a) and 10 μ m (b). (c) Proportion of CeL astrocytes (GS positive cells, left) and neurons (NeuN positive cells, right) positive for OTR mRNA (red) ($n_{\text{astrocytes}} = 1185$, $n_{\text{neurons}} = 1254$, $n_{\text{rats}} = 4$). (d) Cells were reconstructed in 3D using Imaris and morphological parameters were evaluated. Scale bar = 20 μ m (e) OTR-expressing astrocytes are bigger and more complex as indicated by several morphological parameters (cell volume, surface, number of processes, process length and domain volume). (f) OTR-expressing astrocytes display a more complex morphology as revealed by Sholl analysis. All data are expressed in mean \pm SEM except for violin plots where hatched line represent the median and the dot lines are the first and third quartiles. *** $p < 0.0001$, student's *t*-test or two-way ANOVA followed by Tukey post-hoc test. (Statistics in Extended Data Table 1).

Figure 2. Astrocytic OTR activation evokes calcium transients in CeL astrocytes of rats and mice. (a) Experimental strategy to express the ChR1/VChR1 chimaera channel rhodopsin variant C1V1 in OTergic neurons (OxytOpto). (b) Experimental scheme of the horizontal CeA slice preparation used, showing C1V1 expressing OT axons (yellow) arising from PVN and projecting to the CeL. (c) Typical traces of relative changes in intracellular calcium in astrocytes (ΔF) induced by the activation of C1V1 in OT axons located in the CeL through 4542 nm light pulses (10 ms width, 30 Hz, duration 20 s). (d) Proportion of responding astrocytes (left), AUC of ΔF traces (middle) and Ca^{2+} transients frequency (right) normalized to baseline values following C1V1 activation in CeL OT axons, $n_{\text{slice}} (n_s) = 7$, $n_{\text{astrocytes}} (n_a) = 36$. (e) (left) Images of CeL astrocytes identified through SR101 (red, top) and corresponding pseudo-color images of OGB1 fluorescence during baseline and after drug application (middle, bottom, stacks of 50 images over 25s of recording). Scale bar = 10 μ m. (right) Typical ΔF traces following TGOT+TTX (Ctrl) application (f) Proportion of responding astrocytes (left), AUC of ΔF traces (middle) and Ca^{2+} transients frequency (right) normalized to baseline values following application of TGOT (0.4 μ M) with TTX (1 μ M) (Ctrl, $n_s = 18$, $n_a = 136$), without TTX (No TTX, $n_s = 7$, $n_a = 43$), and with an OTR antagonist (dOVT, 1 μ M; $n_s = 3$, $n_a = 24$). Data are expressed as means across slices plus SEM (g) Experimental strategy for the specific deletion of OTRs in mice CeL astrocytes. (h) (left) Example pictures of OTR mRNA (red) and GS (green) labelling in mice injected with PGFAP-GFP-IRES-Cre (top) or PGFAP-GFP rAAV vector (bottom) ; (right) Proportion of CeL astrocytes (GS positive cells) also positive for OTR mRNA (left, blue, PGFAP-GFP: $n_{\text{astrocytes}} = 1340$, $n_{\text{mice}} = 3$; right, red PGFAP-GFP-IRES-Cre: $n_{\text{astrocytes}} = 1561$, $n_{\text{mice}} = 4$). Scale bar = 50 μ m. (i) Proportion of responding astrocytes (left), AUC of ΔF traces (middle) and Ca^{2+} transients frequency (right) normalized to baseline values following application of TGOT+TTX in control (blue, $n_s = 12$, $n_a = 237$) or GFAP OTR KO mice (red, $n_s = 5$, $n_a = 47$; red) acute brain slices. Calcium imaging data are expressed as means across slices plus SEM and white circles indicate averages across astrocytes per slices. * $p < 0.05$, ** $p < 0.01$, *** $p < 0.001$, Unpaired *t*-test or Mann-Whitney U test. (Statistics in Table Extended Data Table 2).

737 **Figure 3. OTR-expressing CeL astrocytes are positioned to recruit a CeL astrocyte**
738 **network through gap junction.** (a) (left) The distance between two OTR+ astrocytes is
739 larger than the distance between two OTR- astrocytes. (right) OTR+ astrocytes
740 predominantly form contacts with OTR- astrocytes, ($n_{\text{astrocytes}} = 1270$, $n_{\text{OTR+ astrocytes}} = 236$, $n_{\text{rats}} = 4$).
741 Contacts are defined by a proximity of less than $1\mu\text{m}$ between GFAP-positive
742 fibers/endfeet from two different astrocytes. (b) (left) Typical ΔF traces following TGOT+TTX
743 application in presence of CBX ($100\ \mu\text{M}$, top) or PPADS ($50\ \mu\text{M}$, bottom). (right) Proportion
744 of responding astrocytes, AUC of ΔF traces and Ca^{2+} transients frequency normalized to
745 baseline values following application of TGOT+TTX ($0.4\ \mu\text{M}$) in presence of CBX ($n_s = 9$, $n_a =$
746 75) or PPADS ($n_s = 7$, $n_a = 53$). (c) (left) Typical ΔF traces following TGOT+TTX application in
747 Cx30/Cx43 KO mice brain slices. (right) Proportion of responding astrocytes, AUC of ΔF
748 traces and Ca^{2+} transients frequency normalized to baseline values following TGOT+TTX
749 application in WT mice ($n_s = 19$, $n_a = 78$) and in Cx30/Cx43 KO mice acute brain slices ($n_s =$
750 17 , $n_a = 100$). Calcium imaging data are expressed as means across slices plus SEM and
751 white circles indicate averages across astrocytes per slices. $*p < 0.05$, $**p < 0.01$, $***p <$
752 0.001 , unpaired t -test or Mann-Whitney U test. (Statistics in Table Extended Data Table 3).
753

754 **Figure 4. CeL astrocyte activity promotes excitatory transmission into CeL neurons.**
755 (a) Experimental strategy for the specific expression of C1V1 in mice CeL astrocytes
756 (AstrOpto). (b) Experimental scheme of the horizontal CeA slice preparation used, showing a
757 C1V1 expressing astrocytes and a patched CeL neuron, recorded in whole-cell voltage-
758 clamp configuration with bath-applied TTX and bicuculline to isolate mEPSC. (c) (left)
759 Proportion of responding astrocytes, AUC of ΔF traces and Ca^{2+} transients frequency
760 following AstrOpto activation ($n_s = 12$, $n_a = 49$) (right) Typical ΔF traces following AstrOpto
761 activation. (d) Frequency of mEPSCs in CeL neurons before (basal), during (AstrOpto) and
762 after (Wash) AstrOpto activation ($\lambda 542\ \text{nm}$, 3 min long, 1 s width pulse at 0,5 Hz; $n = 17$). (e)
763 Example of an astrocyte in CeL patched with a BAPTA-Biocytin filled capillary (white arrow).
764 Biocytin can be seen diffusing in neighboring astrocytes. (f) Frequency of mEPSCs in CeL
765 neurons before (basal), during (TGOT, $0.4\ \mu\text{M}$) and after (Wash) TGOT application (left,
766 $n=16$). This effect can be blocked by loading BAPTA in the CeL astrocyte network (middle,
767 BAPTAstro, $n= 11$) and by prior incubation of an NMDAR antagonist (right, AP5, $50\ \mu\text{M}$, $n =$
768 9). (g) Experimental strategy for the specific deletion of OTRs in mice CeL astrocytes. (h)
769 Frequency of mEPSCs in CeL neurons before (basal), during (TGOT, $0.4\ \mu\text{M}$) and after
770 (Wash) TGOT application in acute brain slice from WT (left, blue, $n = 10$) and from GFAP
771 OTR KO mice (right, red, $n= 8$). Calcium imaging data are expressed as means across
772 slices plus SEM and white circles indicate averages across astrocytes per slices. Patch-
773 clamp data are expressed as averaged frequency plus SEM across cells, linked white circles
774 indicate individual cell values, example traces of the various conditions are displayed on the
775 right. $\#p < 0.05$, $###p < 0.001$, Friedman and Dunn's Multiple comparisons, $*p < 0.05$, $**p <$
776 0.01 , Unpaired t -test or Mann-Whitney U test. (Statistics in Table Extended Data Table 4).
777

778 **Figure 5. CeL astrocyte activity promotes CeL neuron firing.** (a) Experimental strategy
779 for the specific expression of C1V1 in mice CeL astrocytes (AstrOpto) (b) Experimental
780 scheme of the horizontal CeA slice preparation used, showing a C1V1 expressing astrocytes
781 and a patched CeL neuron, recorded in whole-cell current-clamp configuration to record
782 action potentials (APs). (c) Frequency of APs in CeL neurons before (basal), during
783 (AstrOpto) and after (Wash) AstrOpto activation ($\lambda 542\ \text{nm}$, 3 min long, 1 s width pulse at 0,5
784 Hz) in control condition (left, $n = 10$) or following BAPTA loading in the CeL astrocyte network

785 (right, BAPTastro, n = 12). **(d)** Frequency of APs in CeL neurons before (basal), during
786 (TGOT, 0.4 μ M) and after (Wash) TGOT application (left, n = 9). This effect can be blocked
787 by loading BAPTA in the CeL astrocyte network (middle, BAPTastro, n = 9) and by prior
788 incubation of the NMDAR antagonist AP5 (right, AP5, 50 μ M, n = 7). **(e)** Experimental
789 strategy for the specific deletion of OTRs in mice CeL astrocytes (GFAP OTR KO). **(f)**
790 Frequency of APs in CeL neurons before (basal), during (TGOT, 0.4 μ M) and after (Wash)
791 TGOT application in acute brain slices from WT (left, blue, n = 7) and GFAP OTR KO mice
792 (right, red, n = 11). Example traces of the various conditions are displayed on the right.
793 Patch-clamp data are expressed as averaged frequency plus SEM across cells; linked white
794 circles indicate individual cell values. # p < 0.05, ## p < 0.01, Friedman and Dunn's Multiple
795 comparisons, * p < 0.05, *** p < 0.001, Unpaired t -test or Mann-Whitney U test. (Statistics in
796 Table Extended Data Table 5).

797

798 **Figure 6. Astrocyte-driven CeL neuron activity modifies amygdala output.** **(a)**
799 Experimental strategy for the specific expression of C1V1 in mice CeL astrocytes (AstrOpto)
800 **(b)** Experimental scheme of the horizontal CeA slice preparation used, showing a C1V1
801 expressing astrocytes and a patched CeM neuron, recorded in whole-cell voltage-clamp
802 configuration to record IPSCs. **(c)** Frequency of IPSCs in CeL neurons before (basal), during
803 (AstrOpto) and after (Wash) AstrOpto activation (λ 542 nm, 3 min long, 1 s width pulse at 0,5
804 Hz) in control condition (left, n = 19) or following BAPTA loading in the CeL astrocyte network
805 (right, BAPTastro, n = 9). **(d)** Frequency of IPSCs in CeL neurons before (basal), during
806 (TGOT, 0.4 μ M) and after (Wash) TGOT application (left, n = 17). This effect can be blocked
807 by loading BAPTA in the CeL astrocyte network (middle, BAPTastro, n = 17) and by prior
808 incubation of the NMDAR antagonist AP5 (right, AP5, 50 μ M, n = 5). **(e)** Experimental
809 strategy for the specific deletion of OTRs in mice CeL astrocytes (GFAP OTR KO). **(f)**
810 Frequency of APs in CeL neurons before (basal), during (TGOT, 0.4 μ M) and after (Wash)
811 TGOT application in acute brain slices from WT (left, blue, n = 27) and GFAP OTR KO mice
812 (right, red, n = 15). Example traces of the various conditions are displayed on the right.
813 Patch-clamp data are expressed as averaged frequency plus SEM across cells; linked white
814 circles indicate individual cell values. # p < 0.05, #### p < 0.001, Friedman and Dunn's Multiple
815 comparisons, * p < 0.05, ** p < 0.01, *** p < 0.001, Unpaired t -test or Mann-Whitney U test.
816 (Statistics in Table Extended Data Table 6).

817

818 **Figure 7. CeL astrocytes modulate CeA behavioral correlates of comfort and are**
819 **required for their OTR-mediated modulation.** **(a, e)** Experimental strategy for the specific
820 expression of C1V1 in mice CeL astrocytes **(a, AstrOpto)** or the specific deletion of OTRs in
821 mice CeL astrocytes **(e, GFAP OTR KO)**. The treatments applied are color coded as the
822 legend key indicate. Control indicate a vehicle injection. **(b, f)** 4 weeks after the SNI surgery,
823 mechanical pain threshold was assessed on the neuropathic paw before (Ctrl) and at
824 different time points after either TGOT injection or C1V1 activation of CeL astrocytes (gray
825 arrow) for sham (top) and SNI (bottom, gray box) animals **(c, g)** Anxiety levels were
826 assessed through measurements of the time spent in the closed arms of the elevated plus
827 maze after drugs injections or C1V1 light-driven activation of CeL astrocytes for sham (top)
828 and SNI (bottom, gray box). **(d, h)** Conditioned place preference (CPP) was assessed
829 through measurements of the Δ time spent in the paired chamber before and after pairing.
830 Pairing was realized through drugs injections or C1V1 light-evoked activation of CeL
831 astrocytes for sham (top) and SNI (bottom, gray box). Data are expressed as averages
832 across rats or mice plus SEM. n = 4-18 per group (details and statistics in Extended Data

833 Table 7). # $P < 0.001$, ## $P < 0.01$ Wilcoxon signed rank test; * $P < 0.05$, ** $P < 0.01$, *** $P <$
834 0.001 ; ANOVA or mixed-design ANOVA followed by posthoc Bonferroni test (Statistics in
835 Table S7). (i) Oxytocin-dependent cellular interactions in the CeA. We hypothesize that OT
836 released from axons of PVN neurons within the CeL activates OTR+ astrocytes (red) which
837 consequently spread their activation to neighboring OTR- astrocytes (green) through, at least
838 partly, gap junctions. Subsequently, the CeL astrocytes release D-serine which gates the
839 activation of NMDAR on CeL interneurons, ultimately increasing their firing rate. This in turn
840 inhibits CeM output projection neurons, resulting in anxiolysis and the promotion of a positive
841 emotional state.
842

843 METHODS

844

845 Animals

846

847 Animals were housed under standard conditions with food and water available *ad libitum* and
848 maintained on a 12-hour light/dark cycle and all experiments were conducted in accordance
849 with EU rules and approbation from French Ministry of Research (01597.05). For *ex vivo* and
850 *in vivo* experiments, Wistar rats or C5BL/6 mice were used. *Ex vivo* experiments used
851 animals between 18 and 25 days old, except in experiments where rAAVs were injected, in
852 which case animals were between 2 and 6 months old at the time of sacrifice. *In vivo*
853 experiments used 2-month-old animals at the time of the first surgery.

854

855 **Specific deletion of OTRs in CeL astrocytes.** To specifically ablate OTRs in CeA
856 astrocytes, transgenic cKO mice, in which *loxP* sites flank the OTR coding sequence²³,
857 received bilateral injections (280 nl) of rAAV-GFAP-GFP-IRES-Cre. Following four weeks of
858 expression of the viral proteins, mice were intracardially perfused with 1x PBS and 4% PFA.
859 Brain sections were used for FISH (OTR mRNA) and IHC (GS) to verify the validity of the
860 approach. Representative images and quantifications are provided in Figure 2H, Extended
861 Data Fig. 2g-h.

862

863 **Specific deletion of Cx30 and Cx43 in astrocytes.** To specifically impair gap-junctions
864 coupling, we used *Cx30^{-/-}Cx43^{fl/fl}:hGFAP-Cre* mice (*Cx30/Cx43* double KO), which were
865 previously characterized^{24,51,52}, with conditional deletion of *Cx43* in astrocytes⁵³ and
866 additional deletion of *Cx30*⁵⁴.

867

868 Cloning and Production of rAAV Vectors:

869

870 The generation of rAAVs allowing for the specific expression of the protein of interest in OT-
871 cells is described in our previous work⁴. Briefly, the conserved promoter region of 2.6 kb was
872 chosen using the software BLAT from UCSC (<http://genome.ucsc.edu/cgi-bin/hgBlat>), was
873 amplified from BAC clone RP24-388N9 (RPCI-24 Mouse, BACPAC Resources, CHORI,
874 California, USA) and was subcloned into a rAAV2 backbone carrying an Ampicillin-
875 resistance.

876

877 To construct the OTp-C1V1(t/t)-TS-mCherry AAV vector we used previously cloned OTp-
878 DIO-GFP-WRE plasmid² equipped with the characterized 2.6 kb OT promoter⁴. In this
879 plasmid the DIO-GFP sequence was replaced by C1V1(t/t)-TS-mCherry from the rAAV
880 CaMKIIa-C1V1(t/t)-TS-mCherry (Addgene, plasmid #35500).

881

882 To generate GFAP-C1V1(t/t)-TS-mCherry AAV vector, we replaced the CamKIIa promoter
883 from the rAAV CaMKIIa-C1V1(t/t)-TS-mCherry by the Gfa promoter from the pZac2.1
884 gfaABC1D-tdTomato (Addgene, plasmid: 44332). The cell type specificity of the rAAV
885 carrying the Gfa promoter was confirmed⁵⁵. In analogy, the generation of the GFAP-GFP-
886 IRES-Cre vector was achieved using pZac2.1 gfaABC1D-tdTomato (Addgene, plasmid:
887 44332). First, the promoter was cloned into a rAAV2 backbone and sticky ends were blunted
888 with *EcoR1* and *Basrg1*. Next, pAAV-CamKIIa-C1V1(t/t)-TS-mCherry was blunted using
889 *BamHI* and *BsrGI*. Finally, the pBS-ires cre construct was used and IRES-Cre was inserted
890 into the GFAP-driven vector resulting in the GFAP-GFP-IRES-Cre construct.

891

892 Production of chimeric virions (recombinant Adeno-associated virus 1/2; rAAV 1/2) was
893 described in⁴. Briefly, human embryonic kidney cells 293 (HEK293; Agilent #240073) were
894 calcium phosphate-transfected with the recombinant AAV2 plasmid and a 3-helper system.
895 rAAV genomic titers were determined with QuickTiter AAV Quantitation Kit (Cell Biolabs, Inc.,
896 San Diego, California, USA) and are $\sim 10^{13}$ genomic copies per ml for all rAAV vectors used
897 in this study.

898

899 **Surgeries**

900

901 **Neuropathic Pain Model: Spared Nerve Injury (SNI) Procedure**

902

903 Animals were randomly separated in two groups to undergo either posterior left hindpaw SNI
904 or sham procedure, with right hindpaw untouched. Animals were anaesthetized using
905 isoflurane at 1.5–2.5%. Incision was made at mid-thigh level using the femur as a landmark
906 and a section was made through the biceps femoris. The three peripheral branches (sural,
907 common peroneal and tibial nerves) of the sciatic nerve were exposed. Both tibial and
908 common peroneal nerves were ligated using a 5.0 silk suture and transected. The sural
909 nerve was carefully preserved by avoiding any nerve stretch or nerve contact²⁸. For animals
910 undergoing sham surgery, same procedure was performed but nerves remained untouched.
911 Animals were routinely observed daily for 7 days after surgery and daily tested by the
912 experimenter (Extended Data Fig. 6). Besides observing weight, social and individual
913 behavior, the operated hindpaw was examined for signs of injury or autotomy. In case of
914 autotomy or suffering, the animal was euthanized in respect of the ethical recommendations
915 of the EU. No analgesia was provided after the surgery in order to avoid interference with
916 chronic pain mechanisms and this is in accordance with our veterinary authorization.
917 Suffering was minimized by careful handling and increased bedding.

918

919 **Stereotaxic Surgery: Injections of rAAV Vectors**

920

921 Stereotaxic surgery was performed under deep ketamine-xylazine anesthesia, using the
922 KOPF (model 955) stereotaxic system. For specific control of rats CeA astroglial cells, 200 nl
923 of rAAV serotype 1/2 (GFAPP-C1V1(t/t)-mCherry, cloned from plasmids #35500 and 44332,
924 Addgene) were injected bilaterally at the coordinates corresponding to CeL: rostro-caudal: -
925 2.7mm, medio-lateral: 4.2mm, dorso-ventral: -8.0mm (From Paxinos and Watson Atlas). For
926 specific control of OT neurons, 200 nl of rAAV serotype 1/2 (OTp-C1V1(t/t)-mCherry or OTp-
927 ChR2-mCherry) were injected bilaterally at the coordinates corresponding to each
928 hypothalamic OT nuclei. PVN: rostro-caudal: -1.8mm; medio-lateral: +/-0.4mm; dorso-ventral:
929 -8.0mm; SON: rostro-caudal: -1.4mm; medio-lateral: +/-1.6mm; dorso-ventral: -9.0mm; AN:
930 rostro-caudal: -2mm; medio-lateral: +/-1.2mm; dorso-ventral: -8.5mm (From Paxinos and
931 Watson Atlas). For specific deletion of OTR in mice CeL astrocytes, 280 nl of rAAV serotype
932 1/2 (GFAPP-GFP-IRES-Cre) were injected bilaterally at the coordinates corresponding to
933 CeL: rostro-caudal: -1.4mm, medio-lateral: +/-2.6mm, dorso-ventral: -4.3mm (From Paxinos
934 and Watson Atlas) in OTR cKO mice.

935

936 **Stereotaxic Surgery: intra-CeL Cannulae**

937

938 **Cannulae Implantation.** Animals were bilaterally implanted with guide cannulae for direct
939 intra-CeL infusions. As guide cannulae we used C313G/Spc guide metallic cannulae
940 (Plastics one, VA, USA) cut 5.8 mm below the pedestal. For this purpose, animals were
941 deeply anesthetized with 4% isoflurane and their heads were fixed in a stereotaxic frame.
942 The skull was exposed and two holes were drilled according to coordinates that were
943 adapted from brain atlas (rat, 2.3 mm rostro-caudal; 4 mm lateral; 7.5 mm dorso-ventral
944 relative to bregma; mice, 1.4 mm rostro-caudal; 2.6 mm lateral; 4.3 mm dorso-ventral relative
945 to bregma) by comparing the typical bregma-lambda distance with the one measured in the
946 experimental animal. Two screws were fixed to the caudal part of the skull in order to have
947 an anchor point for the dental cement. Acrylic dental cement was finally used to fix the
948 cannulae and the skin was sutured. In case of long lasting experiments (neuropathy-induced
949 anxiety) with a cannula implantation at distance of the behavioral assay (> 4 weeks),
950 cannulae were sometimes lost or cloaked, and concerned animals therefore excluded from
951 testing.

952
953 **Drugs Infusions.** We used bilateral injections of 0.5 μ l containing either vehicle (NaCl 0.9%)
954 or oxytocin receptor agonist TGOT (1 μ M) dissolved in NaCl 0.9%. For this procedure two
955 injectors (cut to fit 5.8 mm guide cannulae protruding 2 to 2.5 mm beyond the lower end of
956 the cannula in older animals and 1.8 mm in 3-4 week old rats) were bilaterally lowered into
957 the guide cannula, connected via polythene tubing to two Hamilton syringes that were placed
958 in an infusion pump and 0.5 μ l of liquid was injected in each hemisphere over a 2-minute
959 period. After the injection procedure, the injectors were kept in place for an additional minute
960 in order to allow a complete diffusion of liquid throughout the tissue. Rats were subsequently
961 left in the home cage for 15 minutes to recover from the stress of the injection and then
962 handled for mechanical pain threshold or anxiety assessment. Animals that received TGOT
963 injections for the first experiment (mechanical sensitivity assessment) were switched to the
964 vehicle injected groups for the elevated plus maze experiment.

965 966 **Stereotaxic Surgery: intra-CeL Optical Fiber**

967
968 **Optical Fiber Implantation.** Sham and rAAVs injected animals both underwent a single
969 surgical procedure in which after vector injection or no injection for sham, optical fibers
970 designed to target the CeL were implanted and firmly maintained on the skull using dental
971 cement. See "**cannulae implantation**" for the surgical procedure. Implantable optical fibers
972 were homemade using optical fiber cut at appropriate length (FT200EMT, Thorlabs, NJ,
973 USA) inserted and glued using epoxy based glue in ferrules (CFLC230-10, Thorlabs, NJ,
974 USA).

975 976 **Horizontal and Coronal Slices**

977
978 **Slices Preparations.** In all cases, animals were anaesthetized using ketamine (Imalgene 90
979 mg/kg) and xylazine (Rompun, 10 mg/kg) administered intraperitoneally. Intracardiac
980 perfusion was then performed using one of the following artificial cerebrospinal fluids
981 (aCSFs) dissection solutions. For animals between 18 and 25 days old, an ice-cold sucrose
982 based dissection aCSF was used containing (in mM): Sucrose (170), KCl (2.5), NaH₂PO₄
983 (1.25), NaHCO₃ (15), MgSO₄ (10), CaCl₂ (0.5), HEPES (20), D-Glucose (20), L-Ascorbic acid
984 (5), Thiourea (2), Sodium pyruvate (3), N-Acetyl-L-cysteine (5), Kynurenic acid (2). For
985 animals between 2 and 6 months old, an ice-cold NMDG based aCSF was used containing

986 (in mM): NMDG (93), KCl (2.5), NaH₂PO₄ (1.25), NaHCO₃ (30), MgSO₄ (10), CaCl₂ (0.5),
987 HEPES (20), D-Glucose (25), L-Ascorbic acid (5), Thiourea (2), Sodium pyruvate (3), N-
988 Acetyl-L-cysteine (10), Kynurenic acid (2). In both cases, pH was adjusted to 7.4 using either
989 NaOH or HCl, this after bubbling in 95% O₂-5% CO₂ gas, bubbling which was maintained
990 throughout the duration of use of the various aCSFs. Those aCSFs formulae were based on
991 the work of⁵⁶. Following decapitation, brain was swiftly removed in the same ice-cold
992 dissection aCSFs as for intracardiac perfusion, and 350 μm thick horizontal slices containing
993 the CeA was obtained using a Leica VT1000s vibratome. For experiments in Extended Data
994 Fig. 2a-b, coronal slices of the same thickness containing the PVN were used. Upon slicing,
995 brain slices were hemisected and placed, for 1 hour minimum before any experiments were
996 conducted, in a room tempered holding chamber, containing normal aCSFs. For 2 to 6 month
997 old animals, slices were first let for 10 minutes in 35°C NMDG aCSF before placing them in
998 the holding chamber at room temperature. Normal aCSF, also used during all *ex vivo*
999 experiments, is composed of (in mM): NaCl (124), KCl (2.5), NaH₂PO₄ (1.25), NaHCO₃ (26),
1000 MgSO₄ (2), CaCl₂ (2), D-Glucose (15), adjusted for pH values of 7.4 with HCL or NaOH and
1001 continuously bubbled in 95% O₂-5% CO₂ gas. All aCSFs were checked for osmolality and
1002 kept for values between 305-310 mOsm/L. In electrophysiology or calcium imaging
1003 experiments, slices were transferred from the holding chamber to an immersion recording
1004 chamber and superfused at a rate of 2 ml/min with normal aCSFs unless indicated otherwise.
1005

1006 **Drug Application.** OTR agonists were bath applied through a 20s long pumping of agonist
1007 solution, corresponding to several times the volume of the recording chamber. Other drugs
1008 (antagonists, TTX, *etc.*) were applied for at least 20 minutes in the bath before performing
1009 any experiments. BAPTA (or BAPTA-free solution for controls) loading of CeL astrocytes was
1010 realized following⁵⁷ protocol. Two distant CeL astrocytes per slice (label with SR101, 1 μM)
1011 were patched in whole cell configuration and voltage steps were applied (2 Hz, Δ40 mV) to
1012 help loading the BAPTA contained in the patch pipette (in mM): MgCl₂ (1), NaCl (8), ATPNa₂
1013 (2) GTPNa₂ (0.4) HEPES (10), BAPTA (40) and osmolality checked to be between 275-285
1014 mOsm/l. The whole cell configuration was maintained during 45 min to allow BAPTA diffusion
1015 into the astrocyte network⁵⁸.
1016

1017 **Calcium Imaging and Identification of Astrocytes**

1018 To identify astrocytes, SR101 (1 μM) was added to aCSF in a culture well and slices were
1019 incubated for 20 minutes at 35°C. The specificity of SR101 labelling to astrocytes of the CeL
1020 was verified through patch-clamp experiments, the results of which can be found in Extended
1021 Data Fig. 2c-d. The synthetic calcium indicators OGB1 or Rhod-2 was bulk loaded following
1022 an adapted version of the method described previously⁵⁹ reaching final concentrations of
1023 0.0025 % (~20 μM) for calcium indicators, 0.002% Cremophor EL, 0.01 % Pluronic F- 127
1024 and 0.5% DMSO in aCSF, and incubated for 45 to 60 minutes at 38°C. Upon incubation time,
1025 slices were washed in aCSF for at least an hour before any recording was performed.
1026 Astrocytes recorded for this study were those co-labeled, in rats for SR101 and OGB1 and in
1027 mice for GFP and Rhod2. The spinning disk confocal microscope used to perform astrocyte
1028 calcium imaging was composed of a Zeiss Axio examiner microscope with a 40x water
1029 immersion objective (numerical aperture of 1.0), mounted with a X-Light Confocal unit –
1030 CRESTOPT spinning disk. Images were acquired at 2Hz with either a Rolera em-c² emCCD
1031 or an optiMOS sCMOS camera (Qimaging, BC, Canada). Cells within a confocal plane were
1032 illuminated for 100 to 150 ms for each wavelength (SR101 and Rhod-2: 575 nm, OGB1 and
1033 GFP: 475 nm) using a Spectra 7 LUMENCOR. The different hardware elements were

1034 synchronized through the MetaFluor software (Molecular Devices, LLC, Ca, USA) which was
1035 also used for online. Astrocytic calcium levels were measured in hand drawn ROIs
1036 comprising the cell body plus, when visible, proximal processes. In all recordings, the Fiji
1037 rolling ball algorithm was used to increase signal/noise ratio. Further offline data analysis
1038 was performed using a custom written python-based script available on editorial website.
1039 Intracellular calcium variation was estimated as changes in fluorescence signals. To take into
1040 account micro-movements of the specimen on long duration recordings, the fluorescence
1041 values were also calculated for SR101 (or GFP) and subsequently subtracted to the ones of
1042 OGB1 (or Rhod2), except in the case of Figure 2a-d, where astrocytes were identified
1043 through SR101 fluorescence after the recordings, to avoid unwanted stimulation of the C1V1
1044 opsin. On this last case, recordings in which movements / drifts were visible were discarded.
1045 Then, a linear regression and a median filter was applied to each trace. Calcium transients
1046 was detected using the find_peaks function of the SciPy library. More precisely, fluorescence
1047 variation was identified as a calcium peak if its prominence exceeds the standard deviation
1048 (or two times the standard deviation for recordings acquired with the sCMOS camera) and if
1049 the maximum peak value surpasses 50 fluorescence units (or 3 units for sCMOS recordings).
1050 ROI with zero calcium variations were excluded from the analysis. The remaining ROI were
1051 considered as living astrocytes and the number of peaks was quantified before and after the
1052 drug application. All data were normalized according to the duration of the recording and
1053 astrocytes was labelled as “responsive” when their AUC or their calcium transient frequency
1054 was increased by at least 20% after drug application. Because the time post-stimulation is
1055 longer than the baseline (10 min vs 5 min), the probability of observing a spontaneous
1056 calcium peak is stronger post-stimulation. To avoid this bias, astrocytes with only one
1057 calcium peak during the whole recording were not considered as responsive. Finally, all data
1058 were averaged across astrocytes per slice, and this results was used as statistical unit. All
1059 data were expressed as ratio (baseline/drug effect), a ratio of 1 meaning neither an increase
1060 nor a decrease of the measured parameter. For inter-ratio comparison, parametric or non-
1061 parametric (depending on data distribution) unpaired statistical tests were used. Fiji software
1062 was also used on SR101 / OGB1 pictures to produce illustrative pictures. All calcium imaging
1063 experiments was conducted at controlled room temperature (26°C).

1064

1065 **Electrophysiology**

1066

1067 Whole cell patch-clamp recordings of CeL neurons, CeL astrocytes and CeM neurons were
1068 visually guided by infrared oblique light visualization of neurons and completed by SR101
1069 fluorescence observation for astrocytes. Patch-clamp recordings were obtained with an Axon
1070 MultiClamp 700B amplifier coupled to a Digidata 1440A Digitizer (Molecular Devices, CA,
1071 USA). Borosilicate glass electrodes ($R = 3.5 - 7 \text{ M}\Omega$) with inner filament (OD 1.5 mm, ID 0.86
1072 mm; Sutter Instrument, CA USA) were pulled using a horizontal flaming/brown micropipette
1073 puller (P97; Sutter Instrument, CA, USA). Recordings were filtered at 2 kHz, digitized at 40
1074 kHz and stored with the pClamp 10 software suite (Molecular Devices; CA, USA). Analysis of
1075 patch-clamp data were performed using Clampfit 10.7 (Molecular Devices; CA, USA) and
1076 Mini analysis 6 software (Synaptosoft, NJ, USA) in a semi-automated fashion (automatic
1077 detection of events with chosen parameters followed by a visual validation).

1078

1079 **Whole-Cell Recording of CeL Neurons.** Recording pipettes were filled with an intracellular
1080 solution containing (in mM): KMeSO_4 (125), CaCl_2 (2), EGTA (1), HEPES (10), ATPNa_2 (2),
1081 GTPNa_2 (0.3). The pH was adjusted to 7.3 with KOH and osmolality checked to be between

1082 290-295 mOsm/l, adjusted with sucrose if needed. For miniature excitatory post synaptic
1083 currents (mEPSCs) recordings, neurons were recorded in voltage clamp and hold at a
1084 membrane potential of -65 mV. For action potentials (APs) recordings, neurons were
1085 recorded in current clamp and hold at $I = 0$. Series capacitances and resistances were
1086 compensated electronically throughout the experiments using the main amplifier. For
1087 mEPSCs measurements in CeL neurons (Figure 4), whole cell recordings were conducted in
1088 a Mg^{2+} free aCSF, also containing bicucullin (10 μM) and TTX (1 μM) as in⁶⁰. Average
1089 events frequencies per cell were calculated on 20s windows, chosen for TGOT or
1090 photostimulation during maximal effect, as determined by the visually identified maximal
1091 slope of the cumulative plot of the number of events. CeM neurons were classified as TGOT-
1092 responsive when the average event frequency was increased by at least 20% during 20s
1093 after TGOT application when compared to baseline average frequency. Baseline and
1094 recovery frequencies were measured respectively at the beginning and end of each
1095 recording. All patch-clamp experiments were conducted at room temperature.

1096
1097 ***Biocytin Filling of CeL Astrocytes.*** In the lateral part of the central amygdala slices
1098 visualized with infrared-differential contrast optics, astrocytes were identified by their
1099 morphological appearance revealed by SR101 and the absence of action potentials in
1100 response to depolarizing current injections. Cells were patched with pipettes filled with (in
1101 mM) 110 K-Gluconate, 30 KCl, 4 $ATPNa_2$, 10 phosphocreatine, 0.3 $GTPNa_2$, 10 HEPES and
1102 5 biocytin (pH: 7.3; 310 mOsm). After obtaining whole-cell configuration astrocytes were hold
1103 at -80 mV and typical filling time was 45 minutes. Then the pipettes were carefully retracted
1104 and slices were incubated for additional 20 minutes in the oxygenated aCSF before fixation.
1105 Only one cell was filled per slice. Slices with filled cells were immersion-fixed at 4°C for 5
1106 days in 4% PFA-PBS solution. Next, the slices were flat-embedded in 6% Agar-PBS, areas
1107 of interest were cut out of, re-embedded onto the Agar block and Vibratome-cut into 80 μm
1108 thick free-floating sections. The sections then were incubated with Avidin conjugated to Alexa
1109 Fluor488 (1:1000) (Thermo Fisher) in 1% Triton-PBS at 4°C, washed in PBS, mounted and
1110 cover-slipped. The tissue was analyzed and images taken at Leica TCS SP5 Confocal
1111 Microscope.

1112
1113 ***Whole-cell Recording of CeM Neurons.*** Pipettes were filled with an intracellular solution
1114 containing (in mM): KCl (150), HEPES (10), $MgCl_2$ (4), $CaCl_2$ (0.1), BAPTA (0.1), $ATPNa_2$
1115 (2), $GTPNa_2$ (0.3). pH was adjusted to 7.3 with KOH and osmolality checked to be between
1116 290-295 mOsm/L, adjusted with sucrose if needed. All cells were hold at a membrane
1117 potential of -70 mV. Series capacitances and resistances were compensated electronically
1118 throughout the experiments using the main amplifier. Average events frequencies per cell
1119 were calculated on 20s windows, chosen for TGOT or photostimulation during maximal
1120 effect, as determined by the visually identified maximal slope of the cumulative plot of the
1121 number of events. CeM neurons were classified as TGOT-responsive when the average
1122 IPSCs frequency was increased by at least 20% during 20s after TGOT application when
1123 compared to baseline average frequency. Baseline and recovery frequencies were measured
1124 respectively at the beginning and end of each recording. All patch-clamp experiments were
1125 conducted at room temperature.

1126
1127 **Immunohistochemistry and *in situ* Hybridization**

1128

1129 **In situ Hybridization for OTR mRNA in Rat CeL.** The probe for OTR mRNA was *in vitro*
1130 transcribed from a 902-bp fragment containing 133-1034 bases of the rat OTR cDNA (NCBI
1131 Reference Sequence: NM_012871.3) subcloned into pSP73 Vector (Promega). The
1132 digoxigenin (DIG)-labeled antisense and sense RNA probe from the linearized *oxtr* cDNA
1133 template was synthesized using DIG RNA Labeling Kit (SP6/T7) (Roche Diagnostics).
1134 Sections containing 2 consecutive sections of the CeL (corresponding to Bregma: 2.5) were
1135 processed for fluorescent *in situ* hybridization (FISH). Rats were transcardially perfused with
1136 PBS followed by 4% PFA. Brains were dissected out and post fixed overnight in 4% PFA at
1137 4°C with gentle agitation. 50 µm vibratome sections were cut, collected and fixed in 4% PFA
1138 at 4°C overnight. The free-floating sections were washed in RNase-free PBS, immersed in
1139 0.75% glycine in PBS, treated with 0.5 µg/ml proteinase K for 30 min at 37 °C, acetylated
1140 with 0.25% acetic anhydride in 0.1 M triethanolamine, and then hybridized with DIG-labeled
1141 RNA probe overnight at 65 °C. After RNase treatment and following intensive wash, the
1142 hybridized DIG-labeled probe was detected by incubation with Anti-Digoxigenin-POD (1:200;
1143 11207733910; Roche Diagnostics) for 3 days at 4 °C. Signals were developed with tyramid
1144 signal amplification method. Rhodamine-conjugated tyramide was synthesized by coupling
1145 NHS-Rhodamine (Pierce Biotechnology, Thermo Fisher Scientific) to Tyramine-HCl (Sigma-
1146 Aldrich) in dimethylformamide with triethylamine. For the quantification of OTR mRNA-
1147 positive astrocytes, all confocal images were obtained using the same laser intensities and
1148 processed with the same brightness / contrast settings in Adobe Photoshop. Since the *in situ*
1149 signal for the OTR mRNA in astrocytes was weak, we first calculated the average intensity
1150 (signal intensity of all pixels divided by the total number of pixels) of the rhodamine-stained
1151 OTR mRNA signal for each individual section containing the CeL. Next, we calculated the
1152 standard deviation for each individual confocal image based on the intensity of all pixels
1153 comprising the image. We defined the threshold for OTR mRNA-positive astrocytes: If more
1154 than 1/4 of all pixels comprising an astrocyte soma displayed a signal intensity exceeding the
1155 average background intensity by more than 4-times the standard deviation, the astrocytes
1156 were considered as OTR mRNA-positive.

1157
1158 **Astrocytes Markers.** The aldehyde dehydrogenase 1 antibody is a commonly used marker
1159 for glial cells, including astrocytes. Therefore, we used the ALDH1L1 for
1160 immunohistochemistry in our initial experimental studies (Extended Data Fig. 1c, S4a).
1161 However, due to inconsistencies in staining quality as a result of batch-dependent antibody
1162 properties, especially in combination with the OTR mRNA FISH, we decided to employ
1163 Glutamine Synthetase (GS, Figure 1). GS is a commonly used glial marker⁶¹, which stains
1164 astrocyte cell bodies, faint processes and even astrocytes not expressing GFAP. Using GS,
1165 we achieved consistent results in combination with our OTR mRNA FISH.

1166
1167 **Glutamine Synthase, ALDH1L1 Colocalization with OTR mRNA in Rat CeL.** After
1168 development and washing steps the sections were stained with antibodies against GS
1169 (mouse monoclonal, 1:500, ref: MAB302, MerckMilipore), ALDH1L1 (rabbit polyclonal, 1:500,
1170 ref: ab87117, abcam), in PBS and kept at 4°C on a shaker in a dark room overnight. After
1171 intensive washing with PBS, sections were stained with the respective secondary antibodies
1172 AlexaFluor488 (goat anti-mouse, 1:1000, ref: A11001, life technologies) and AlexaFluor680
1173 (goat anti-mouse, 1:1000, ref: A27042, ThermoFischer Scientific) for 2 hours at RT.
1174 Following intensive washing with PBS, sections were mounted using Mowiol.

1175

1176 **Double in situ Hybridizations for OTR mRNA and GFAP mRNA in Mice CeL.** Fluorescent
1177 *in situ* hybridization (FISH) in Extended Data Fig. 1d was performed on 25- μ m cryostat-cut
1178 coronal sections prepared from fresh-frozen mouse brain (male C57BL/6J, P22). After
1179 extraction, brains were immediately frozen in Tissue-Tek O.C.T. compound and stored at -80
1180 degrees Celsius. ISH was performed according to the manufacturer's instructions (Advanced
1181 Cell Diagnostics) for Fresh Frozen RNAscope Multiplex Fluorescent Assay. Treatment of
1182 amygdala containing sections were adjusted with the 3-plex negative control and then
1183 coexpression of OTR and GS examined using ACD designed target probes as well as the
1184 nuclear stain DAPI. Single plan images were collected with an upright laser scanning
1185 microscope (LSM-710, Carl Zeiss) using a 40x-objective with keeping acquisition parameters
1186 constant between control and probe treated sections.

1187
1188 **AAV-GFAP-C1V1(*tt*)-mCherry Specificity.** After 3 weeks of vector expression in the brain,
1189 rats were transcardially perfused with 4% paraformaldehyde solution. Tissue blocks,
1190 containing CeA were dissected from the fixed brain and Vibratome-cut into 50 μ m thick free-
1191 floating sections. After several rinse steps sampled sections were blocked with 5% NGS in
1192 PBS and incubated for 48 h at 4°C with polyclonal rabbit anti-ALDH1L1 antibody (1:500,
1193 Abcam) in 1% Triton-PBS buffer, containing 0,1 % NGS. Appropriate secondary antibody
1194 (AlexaFluor488 conjugated goat anti-rabbit (1:1000, LifeTechnologies) was used for further
1195 antigen detection. Intrinsic mCherry fluorescence of vector-expressing cells was strong
1196 enough to detect them in the tissue without any additional antibody enhancement. The
1197 immunolabeled sections were mounted onto Superfrost slides, cover-slipped with Mowiol,
1198 analyzed and documented using LEICA SP5 confocal microscope.

1199
1200 **Three-dimensional assessment of astrocyte complexity and interaction analysis using**
1201 **Imaris.** For the 3D reconstruction of astrocytes, we took Z-stack images (50 μ m depth, 1 μ m
1202 steps, 40x magnification) CeL using a Zeiss LSM 780 confocal microscope (1024x1024 pixel,
1203 16-bit depth, pixel size 0.63-micron, zoom 0.7). Raw czi files were used for further analysis
1204 using Imaris software (Version 9.31, Oxford Instruments). First, Imaris was used to
1205 reconstruct the astrocyte surface using the following custom settings: surfaces Detail 0.700
1206 μ m (smooth); thresholding Background subtraction (Local Contrast), diameter of largest
1207 Sphere, which fits into the object: 2.00; Color: base, diffusion transparency: 65%. After
1208 surface reconstruction, we used the filter function to remove unspecific background signals:
1209 Filter: Volume max – 400 μ m 3. It is important to note that these settings have to be adjusted
1210 for every new batch / IHC staining to guarantee a reliable reconstruction. All astrocytes with
1211 incomplete somata (cut by either the x, y or z plane) were manually removed and not
1212 included in further analysis Fused astrocytes that were falsely recognized as one entity by
1213 the software were manually separated using the cut function, or entirely removed from the
1214 sample if a separation was not feasible. The 'filter/area function' was used to remove small
1215 astrocytic segments that occurred during manual deletion. After deletion of all background
1216 signals the 'mask all' function was used to create the final surface reconstruction. Next, the
1217 surface reconstruction was used as the template for the filament reconstruction using the
1218 following custom settings: detect new starting points: largest Diameter 7.00 μ m, seed points
1219 0.300 μ m; remove seed points around starting points: diameter of sphere regions: 15 μ m.
1220 Seed points were corrected for (either placed in or removed from the center of the somata)
1221 manually if the Imaris algorithm placed them incorrectly. All surface and filament parameters
1222 were exported into separate Excel files and used for data analysis. All images used for
1223 analysis were taken with the same confocal settings (pinhole, laser intensity, digital gain and

1224 digital offset). Sholl analysis was performed using Imaris in the filament reconstruction mode
1225 and individual data sets were exported into separate Excel files for further analysis. each
1226 individual sphere) per individual astrocyte. For the nearest neighbor and interaction analysis
1227 we used the 'Native Distance Measurements' function as depicted in this video:
1228 <https://imaris.oxinst.com/learning/view/article/imaris-9-5-native-distance-measurements>. In
1229 brief, we reconstructed astrocytic surfaces based on the GFAP fluorescence and OTR
1230 mRNA signal. Next, we manually labelled OTR+ and OTR- astrocytes and performed the
1231 native distance measurement allowing us to assess the shortest distance between GFAP-
1232 positive processes of different astrocytes. We defined 'astrocytic interaction' when GFAP-
1233 positive processes of two different astrocytes were no further than 1µm apart. It is important
1234 to note that this method does not allow the discrimination of different astrocytic entities so
1235 that several close contacts (contacts being defined as a distance of less than 1µm between
1236 GFAP-positive processes or endfeets from two different astrocytes) originating from the
1237 same astrocyte result in a higher number of total interactions. For the nearest neighbor
1238 analysis, we calculated the distance from the center of the soma to the nearest astrocyte
1239 neighbor using GS fluorescence and an artificially created sphere that was placed within the
1240 soma and measured the distance accordingly. Distribution plots and correlations as well as
1241 all statistics were performed using GraphPad Prism 8.0.

1242

1243 **Optogenetics**

1244

1245 ***Ex vivo***. We opted for a ChR1/VChR1 chimaera channel rhodopsin displaying a red-shifted
1246 absorption spectrum, referred here as C1V1²². This choice was made over a classical
1247 channelrhodopsin-2 to avoid unwanted stimulation of OT axons while imaging our 488nm
1248 light sensitive calcium indicator (OGB1). Optogenetic green light stimulation of C1V1 in *ex*
1249 *vivo* experiments was performed using either the Spectra 7 LUMENCOR (λ542 nm) or light
1250 source X-Cite® 110LED from Excelitas Technologies through a Cy3 filter, controlled via
1251 MetaFluor or Clampex driven TTL pulses, respectively.

1252

1253 ***In vivo***. Animals were habituated to the fixation of an optical fiber on the ferrule without light
1254 stimulation for one week before the experiment. In all cases, optical fibers were attached to
1255 the ferrules using an adapter (ADAF2, Thorlabs, NJ, USA) and animals let free to move in a
1256 typical home cage for the duration of the stimulation. Implanted optical fibers were connected
1257 to two lasers (LRS-0532-GFM-00100-03 LaserGlow 532nm DPSS Laser System) and the
1258 output power adjusted to correspond to 20 to 30 mW measured at the tip of 200 µm diameter
1259 fibers similar to the one implanted. Stimulation of 500 ms duration at a frequency of 0.5Hz
1260 were given for 3 min.

1261

1262 **Behavior**

1263

1264 ***Mechanical Sensitivity Assessment***. In experiments with rats, we used a calibrated
1265 forceps (Bioseb, Chaville, France) previously developed in our laboratory to test the animal
1266 mechanical sensitivity⁶². Briefly, the habituated rat was loosely restrained with a towel
1267 masking the eyes in order to limit stress by environmental stimulations. The tips of the
1268 forceps were placed at each side of the paw and a graduate force applied. The pressure
1269 producing a withdrawal of the paw, or in some rare cases vocalization, was considered as
1270 the nociceptive threshold value. This manipulation was performed three times for each hind
1271 paw and the values were averaged as being the final nociceptive threshold value. In

1272 experiments with mice, we used von Frey filaments tests. Mechanical allodynia (a symptom
1273 of neuropathic pain) was tested using von Frey hairs and results were expressed in grams.
1274 Tests were performed during the morning starting at least 2 h after lights on. Mice were
1275 placed in clear Plexiglas boxes (7 cm x 9 cm x 7 cm) on an elevated mesh floor. Calibrated
1276 von Frey filaments (Bioseb) were applied to the plantar surface of each hindpaw until they
1277 just bent in a series of ascending forces up to the mechanical threshold. Filaments were
1278 tested five times per paw and the paw withdrawal threshold (PWT) was defined as the lower
1279 of two consecutive filaments for which three or more withdrawals out of the five trials were
1280 observed.

1281

1282 **Elevated Plus Maze.** Following protocol from⁶³, the arena is composed of four arms, two
1283 open (without walls) and two closed (with walls; rats 30 cm high; mice 15 cm high). Arms are
1284 10 cm wide, 50 cm long and elevated 50 cm off the ground for rats and 5 cm wide, 30 cm
1285 long and elevated 40 cm of the ground for mice. Two lamps with intensity adjustable up to 50
1286 watts were positioned on the top of the maze, uniformly illuminating it. Animals were video
1287 tracked using a video-tracking systems (Ethovision Pro 3.16 Noldus, Wageningen,
1288 Netherlands and Anymaze, Stoelting Europe, Ireland). After each trial, the maze was cleaned
1289 with 70% ethanol and dry with paper towel. Twenty minutes after intracerebral injections or
1290 directly after optical stimulation, the animal was let free at the center of the plus maze, facing
1291 the open arm opposite to where the experimenter is, and was able to freely explore the entire
1292 apparatus for six minutes. Total time and time spend in closed and open arms were recorded
1293 in seconds and the percentage of time spent in closed arms was calculated as a measure of
1294 anxiety-like behavior. As internal control, the total distance travelled during the test period
1295 was quantified and compared between all different groups (Extended Data Fig. 7). Animals
1296 falling from the apparatus during the test, freezing more than 50% of the total time, or with
1297 cannulae/optic fiber issues, were removed from the analysis.

1298

1299 **Conditioned Place Preference.** The device is composed of two opaque conditioning boxes
1300 (rats: 30x32 cm; mice: 22x22 cm) and one clear neutral box (30x20 cm) Animals were video
1301 tracked using a video-tracking system (Anymaze, Stoelting Europe, Ireland). After each trial,
1302 the device was cleaned with a disinfectant (Surfa'Safe, Anios laboratory). Based on⁶⁴, all rats
1303 underwent a 3 days habituation period during which they were able to freely explore the
1304 entire apparatus for 30 min. On the day 3, behavior was record for 15 min to verify the
1305 absence of pre-conditioning chamber preference. The time spend in the different
1306 compartment were measured and paired compartment was chosen as the compartment in
1307 which rat spent the less time during the 3rd day of habituation. On day 4, animals were
1308 placed the morning in one compartment for 15 min with no stimulation (unpaired box). Four
1309 hours after, the animal were placed 15 min in the opposite box (paired box) and CeL
1310 astrocyte expressing C1V1 vector were optogenetically stimulated (3 min – 1 s light pulse at
1311 0.5 Hz - λ 542 nm) or TGOT micro-infused through intracerebral cannulae. On day 5, the
1312 animals were place in the CPP box and allowed to freely explore the entire apparatus during
1313 15 min. As internal control, the total distance traveled during the test period was quantified
1314 and compared between all different groups (Extended Data Fig. 7). Rats falling spending
1315 more than 80% of the total time in a single chamber before the conditioning, or with
1316 cannulae/optic fiber issues, were removed from the analysis.

1317

1318 **QUANTIFICATION AND STATISTICAL ANALYSIS**

1319 All parametrical statistical tests presented in figure captions or manuscript were performed
1320 following correct verification of the assumptions on the distribution of data, and if not non-
1321 parametric tests were used. Statistical test displayed in the text are not shown on figures.
1322 Tests were performed using either GraphPad Prism (version 8.0.0 for Windows, GraphPad
1323 Software, San Diego, California USA) or the SciPy Python-based library⁶⁵. All values, group
1324 compositions and statistical tests for each experiment and figure panel are detailed in
1325 Extended Data Tables 1-7.
1326

1327
1328
1329

SUPPLEMENTARY DISCUSSION – TECHNICAL LIMITATIONS

1330 We acknowledged a number of technical limitations in our study, which are discussed in
1331 details here:

1332 **mRNA detection.** It is surprising to find that the loss of OTR expression in astrocytes results
1333 in a loss of function of OTR signaling in the CeA-CeM projection, especially considering the
1334 high proportion of OTR+ neurons (up to 70%) compared to the lower fraction of OTR+
1335 astrocytes (18%) in the CeL. One methodological limitation here is that we remained limited
1336 to measuring mRNA levels through FISH, and could not measure OTR expression at the
1337 protein level, notably due to the poor availability of reliable OTR antibodies. It is also possible
1338 that a comparison between the astrocytes' and neurons' contents of OTR mRNA is biased,
1339 indeed astrocytes have a lower total mRNA contents than neurons, as publicly available
1340 databases of single cell RNA sequencing indicate^{66,67}. Interestingly, a similar discrepancy
1341 between low receptor levels observed in astrocytes compared to neurons and yet a crucial
1342 functional relevance of astrocytes' receptors in neuromodulation is also observed for another
1343 GPCR, the CB1 receptor⁶⁸ (and references therein).

1344

1345 **C1V1 red-shifted opsin to activate astrocytes.** It has been recently demonstrated that the
1346 activation of such depolarizing channel rhodopsins in astrocytes or neurons can lead to a
1347 significant leak of potassium ions in the extracellular space, resulting in increased neuronal
1348 excitability⁶⁹. Yet, we provide results in which we buffered the astrocytes intracellular calcium
1349 using BAPTA infusion before activating astrocytic C1V1, and found that it abolished its
1350 effects on CeA neurons (Fig. 4-6). Furthermore, we demonstrate that the AstrOpto effect on
1351 CeA neuronal circuit is dependent on NMDARs (Extended Data Fig. 5a). This indicates that
1352 consequences of astrocytic C1V1 activation are dependent on the evoked astrocyte calcium
1353 signaling rather than potassium leakage.

1354

1355 **Bulk loading of organic calcium indicator dyes.** It should also be noted that we used bulk
1356 loading of organic calcium indicator dyes. This means we could not precisely measure
1357 cytosolic calcium changes in fine astrocyte processes⁷⁰, which may have revealed more
1358 complex activities of astrocytes. We note it has been proven that endogenous or exogenous
1359 (designer receptor exclusively activated by designer drugs receptors, DREADD) GPCR
1360 signaling in astrocytes produces a global increase in calcium in both the cell body and
1361 processes⁶⁸ and references therein).

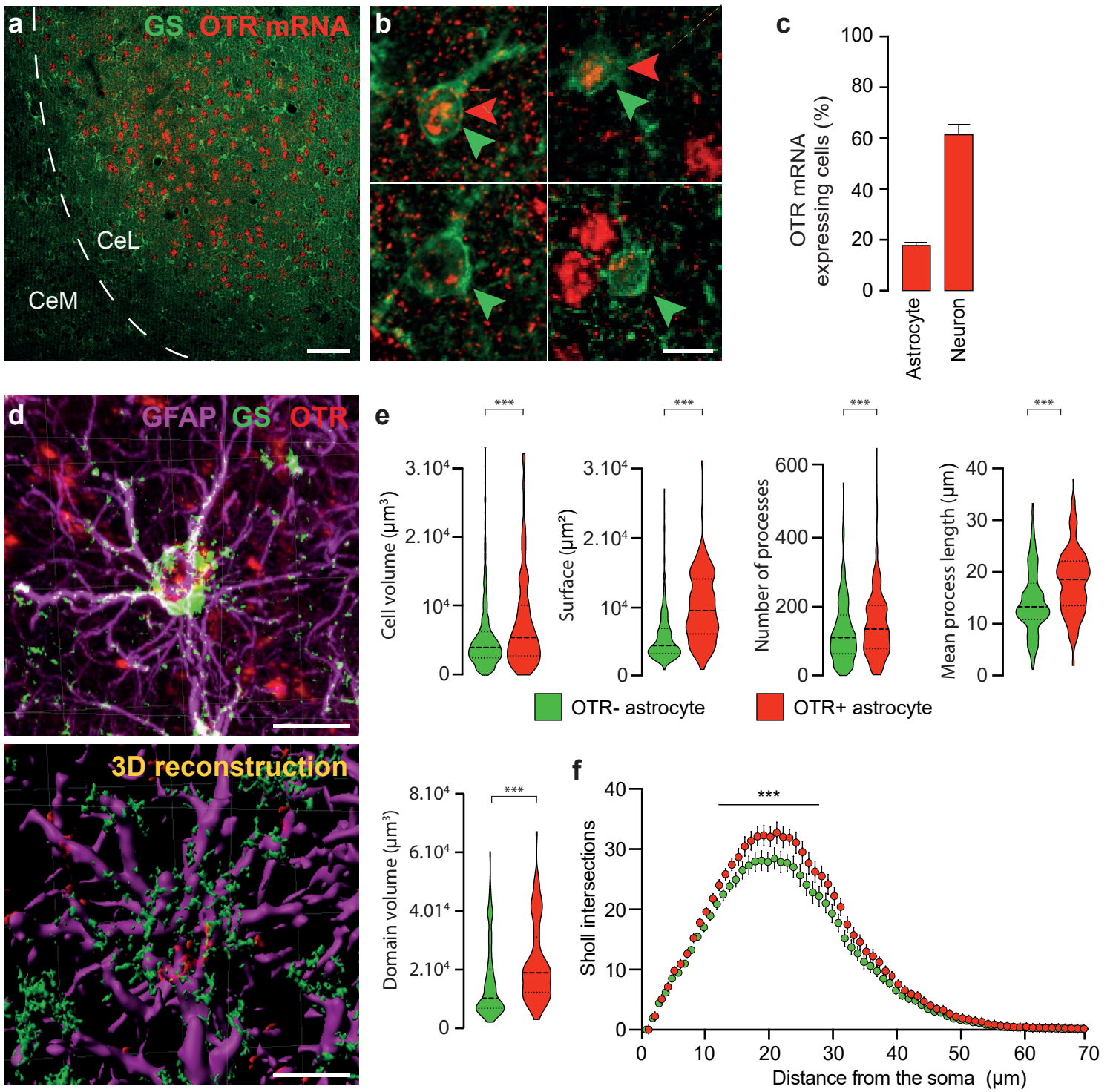


Figure 1

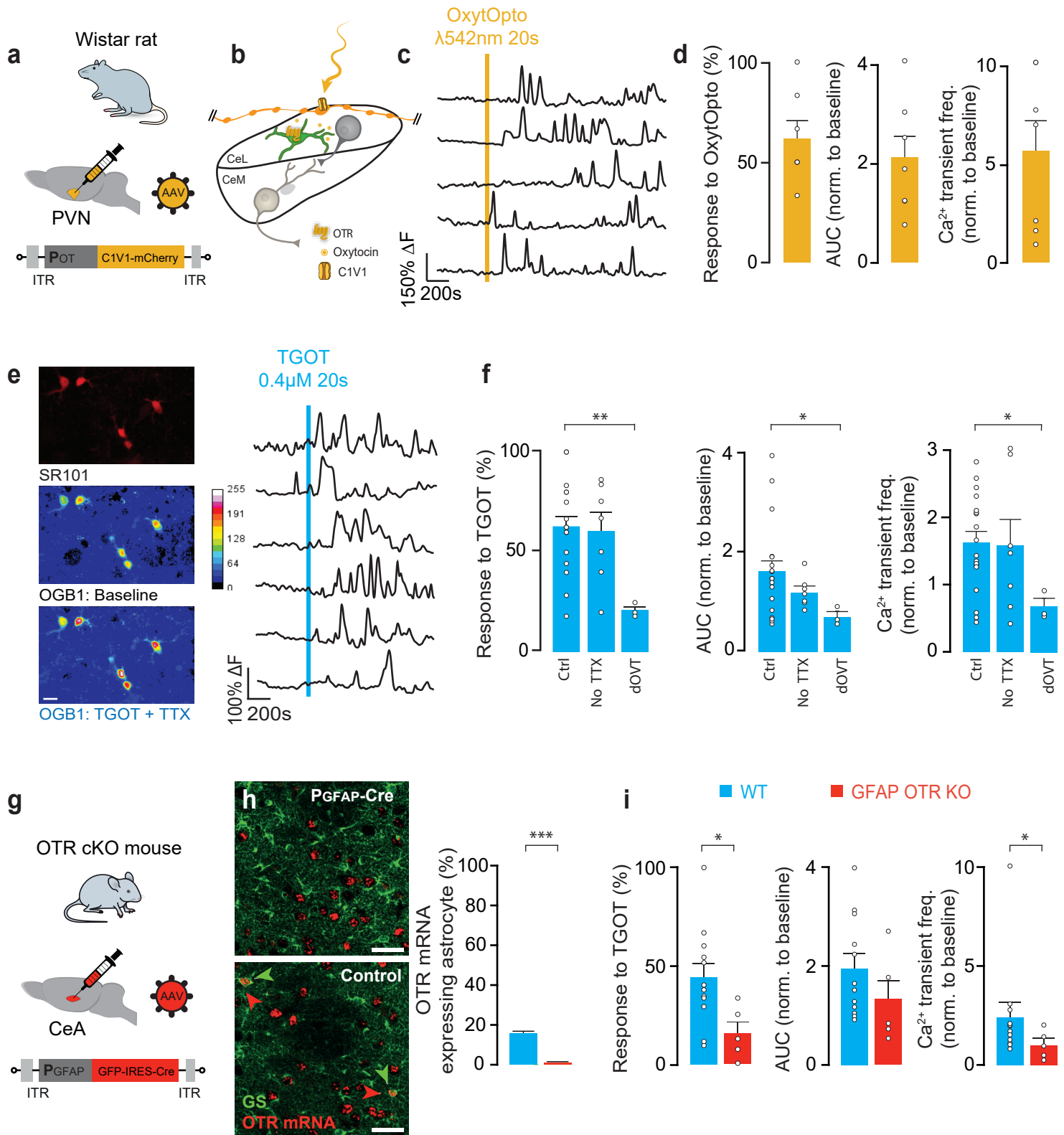


Figure 2

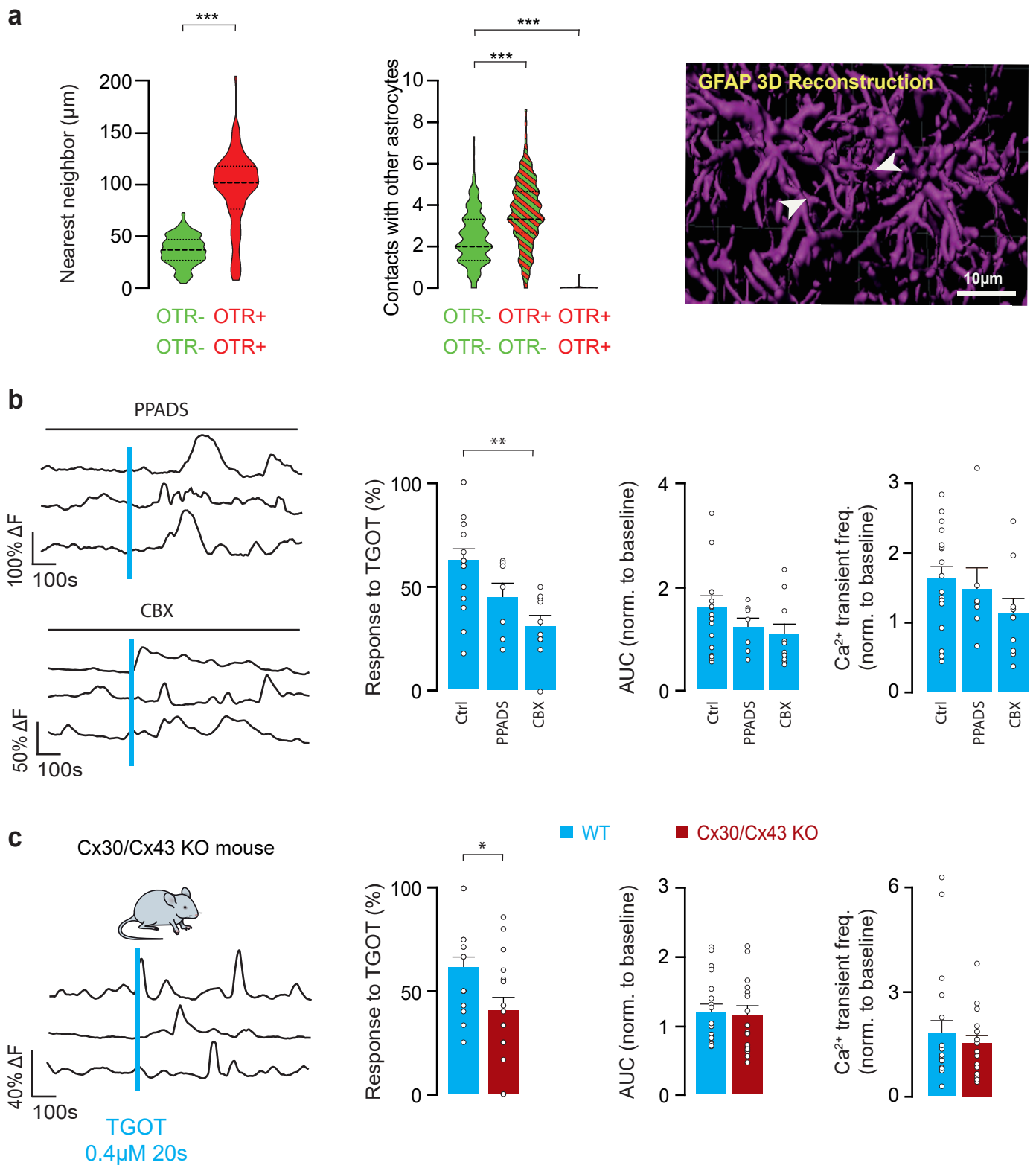


Figure 3

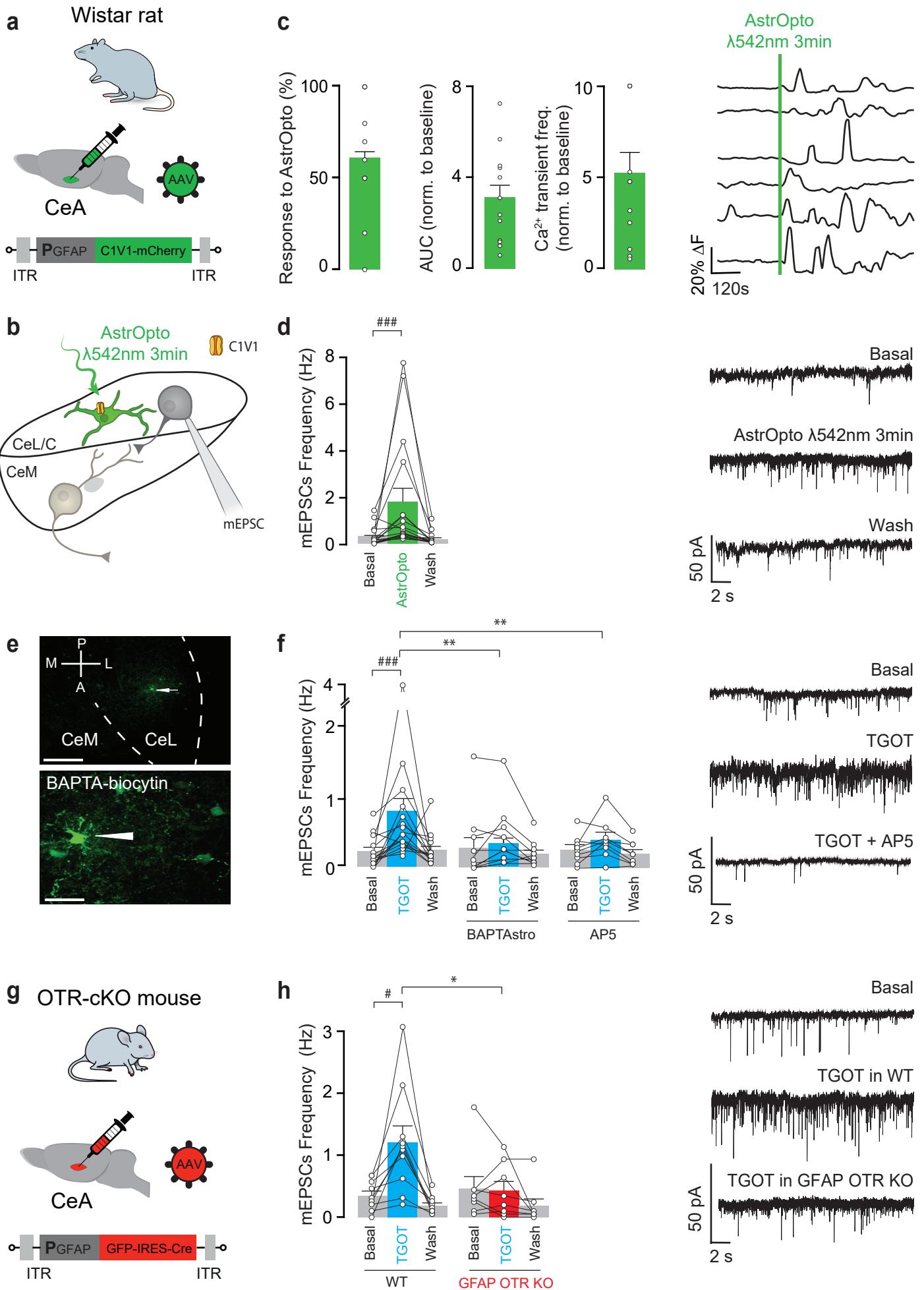


Figure 4

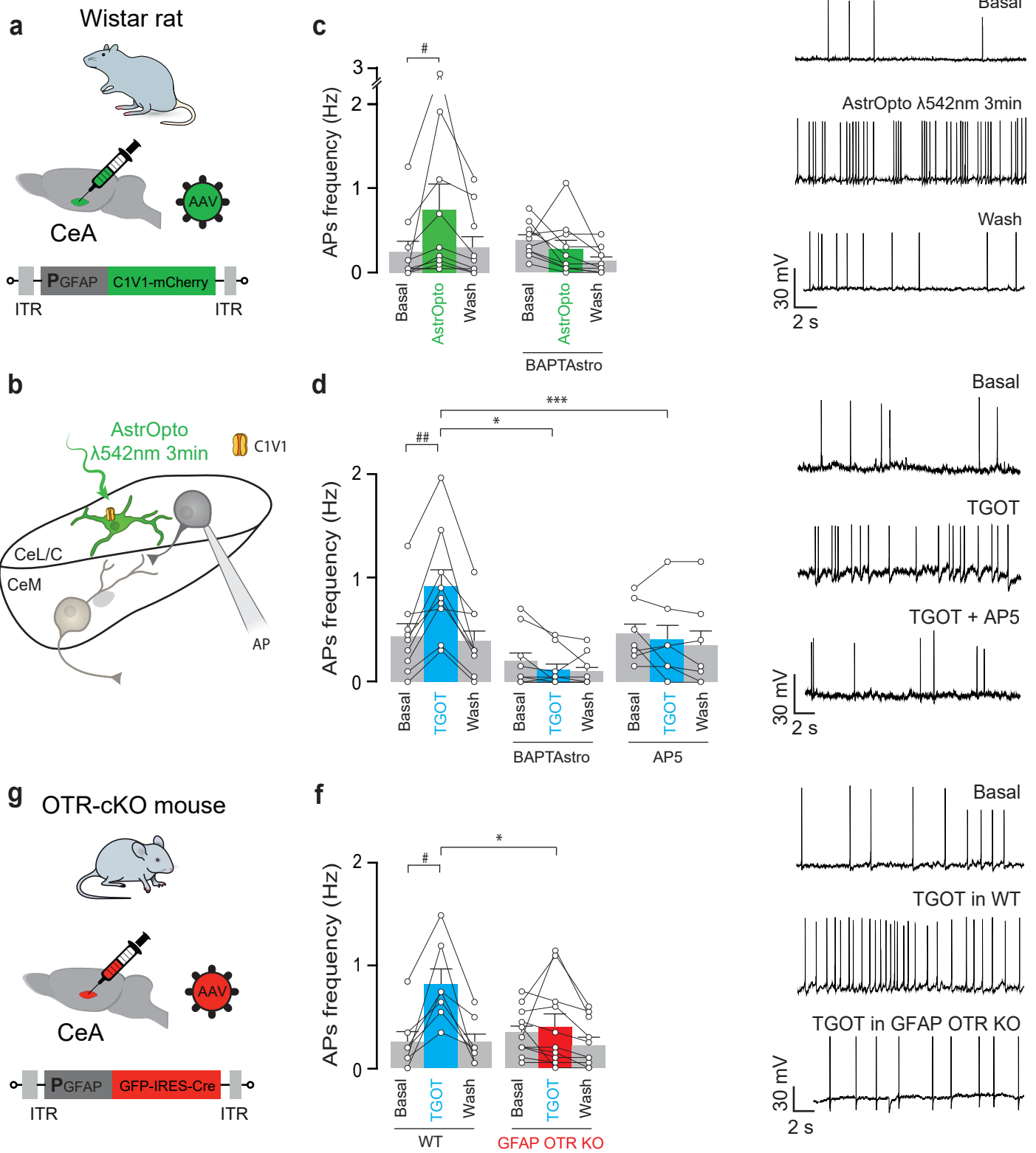


Figure 5

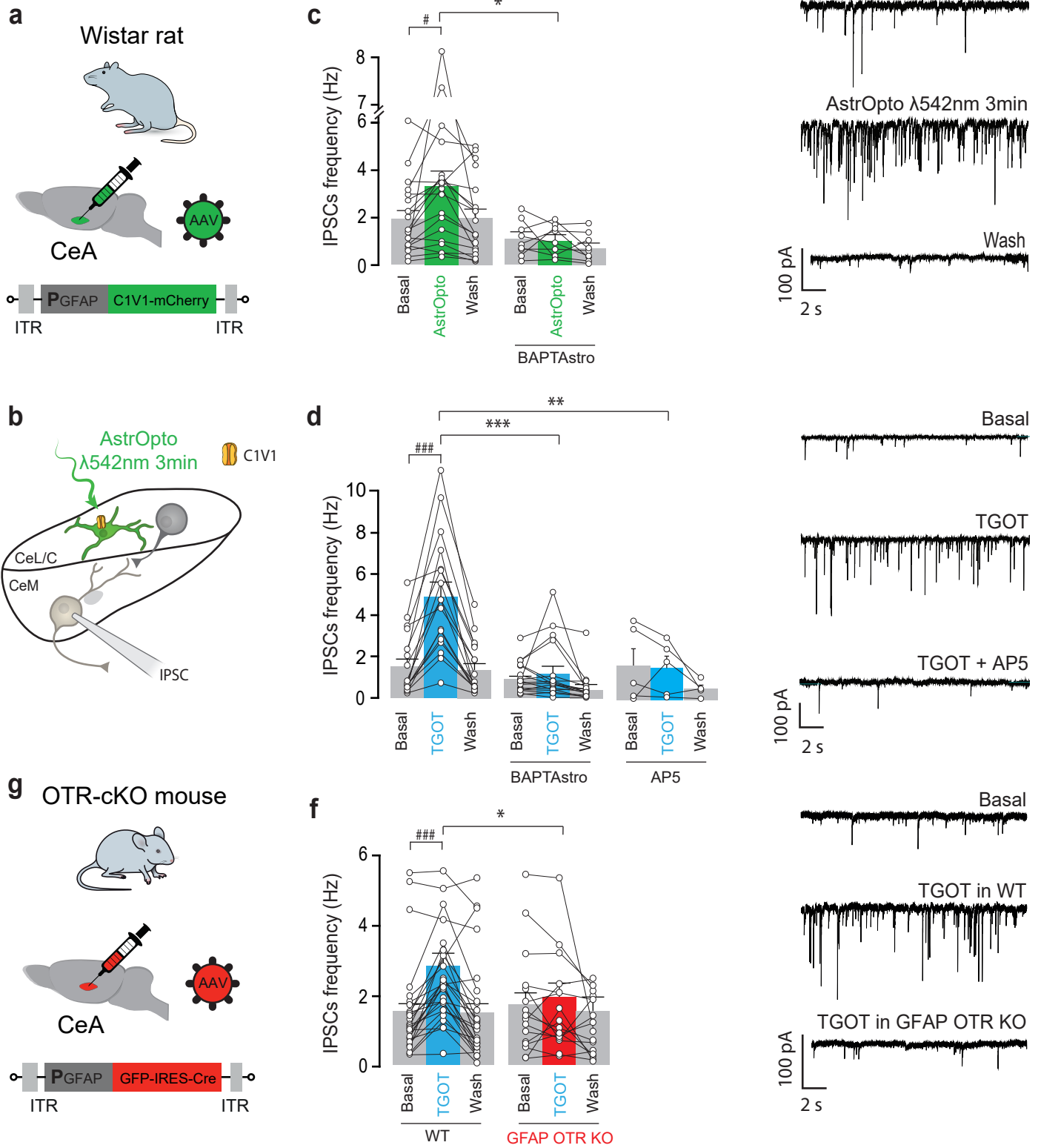
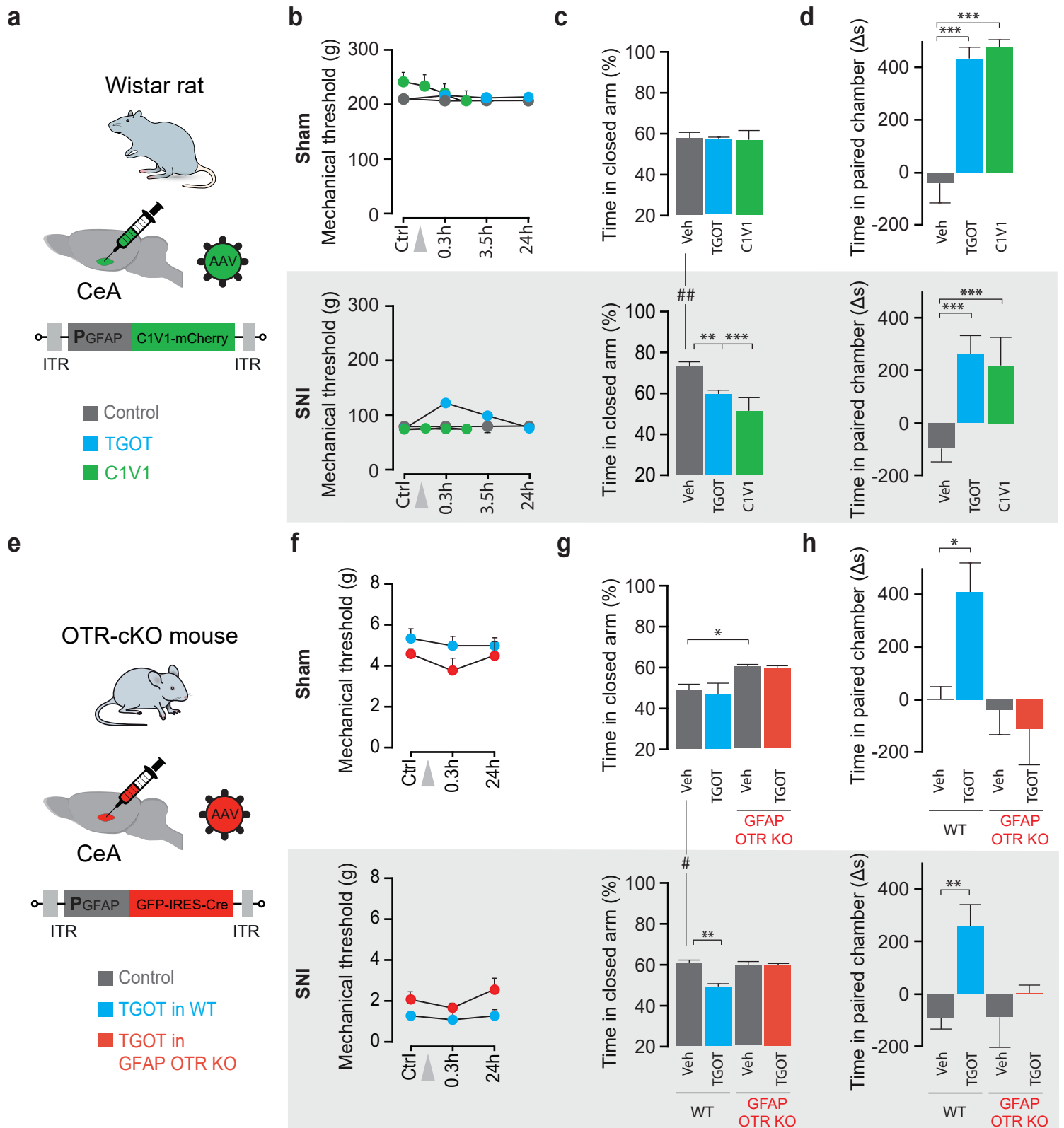


Figure 6



i

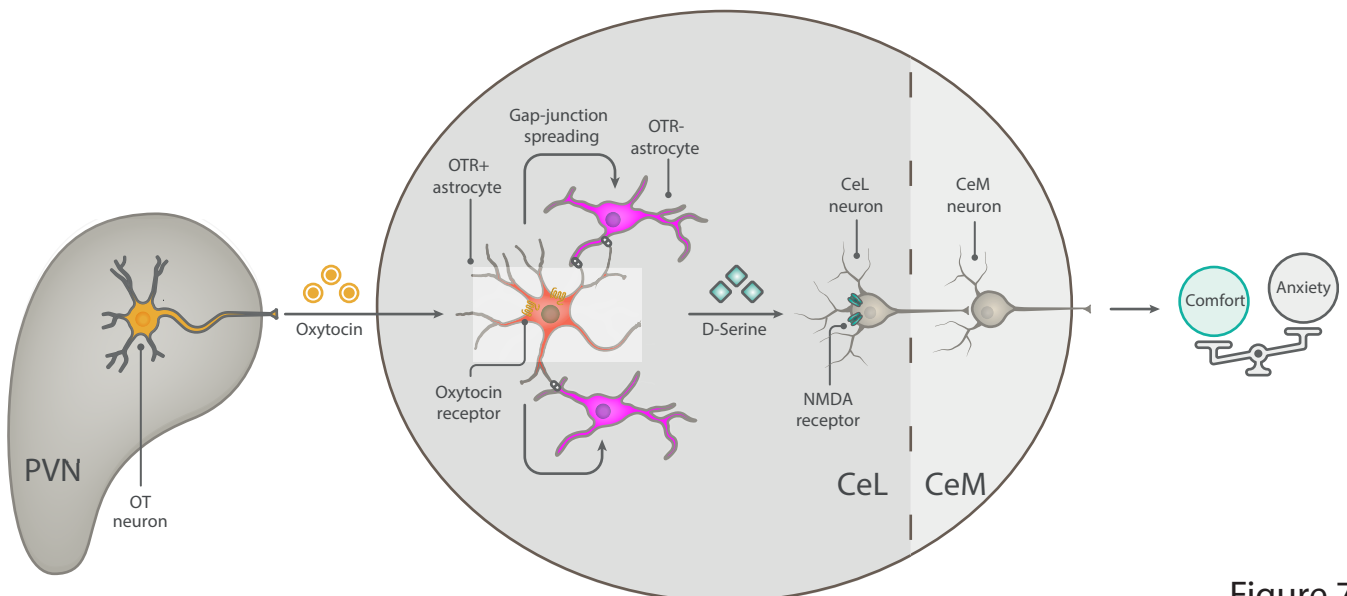
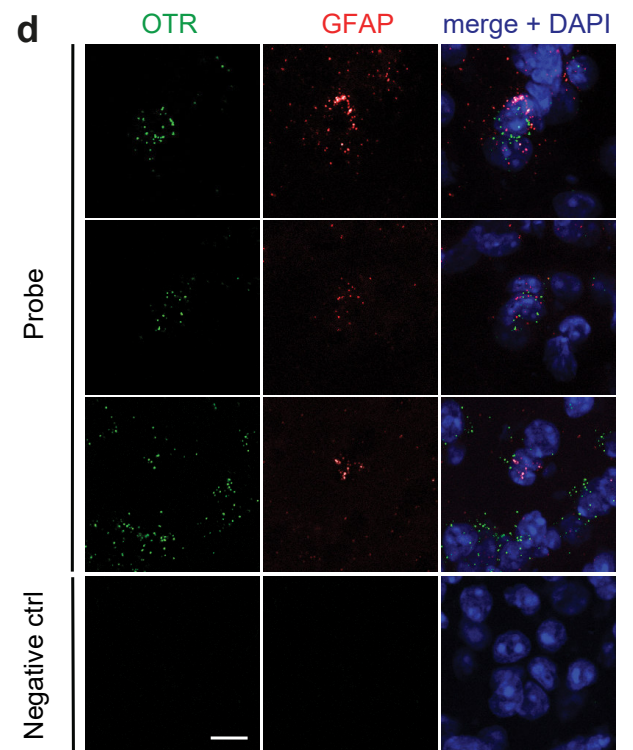
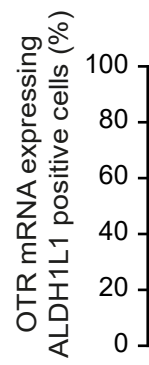
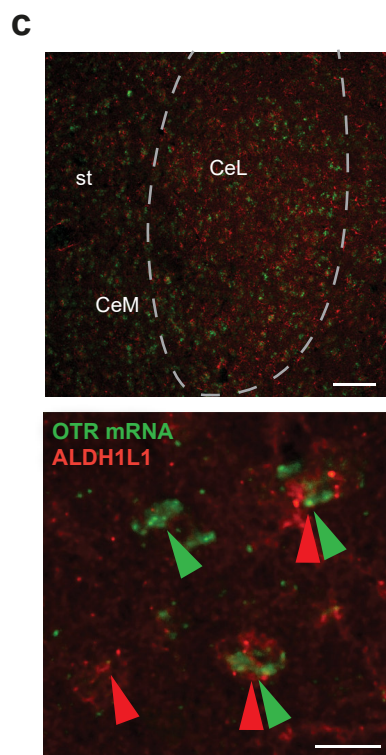
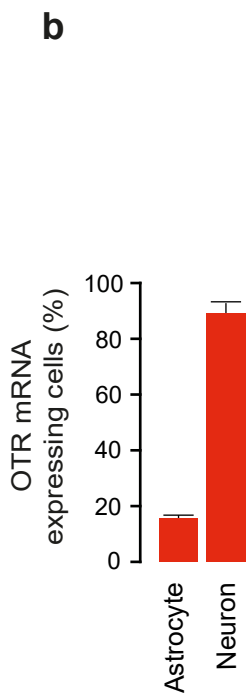
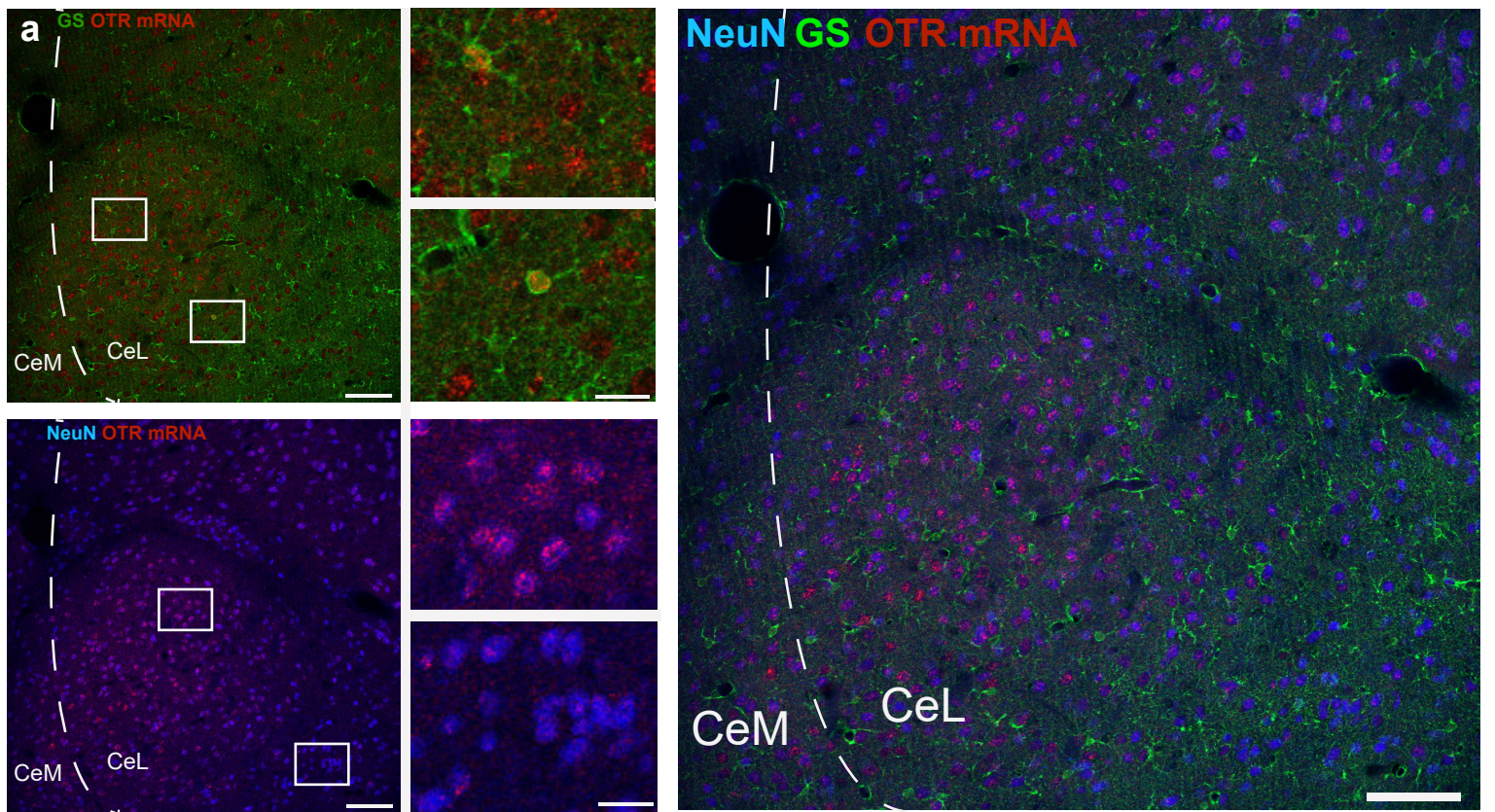
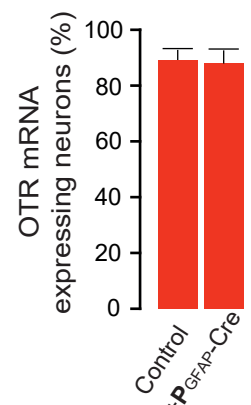
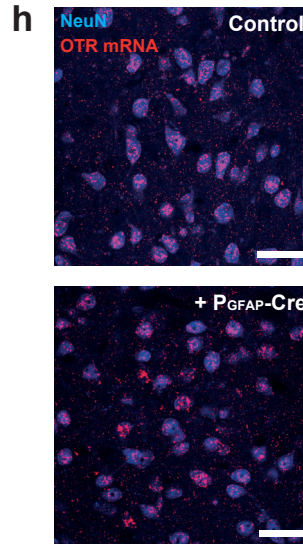
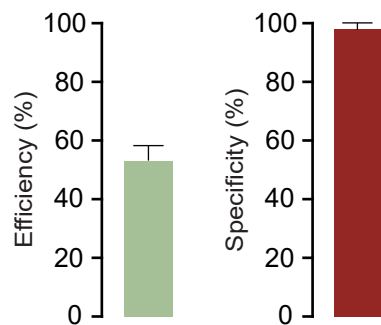
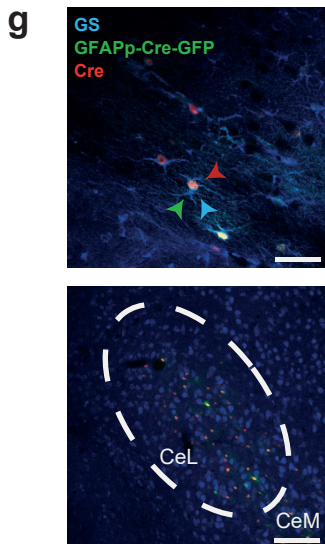
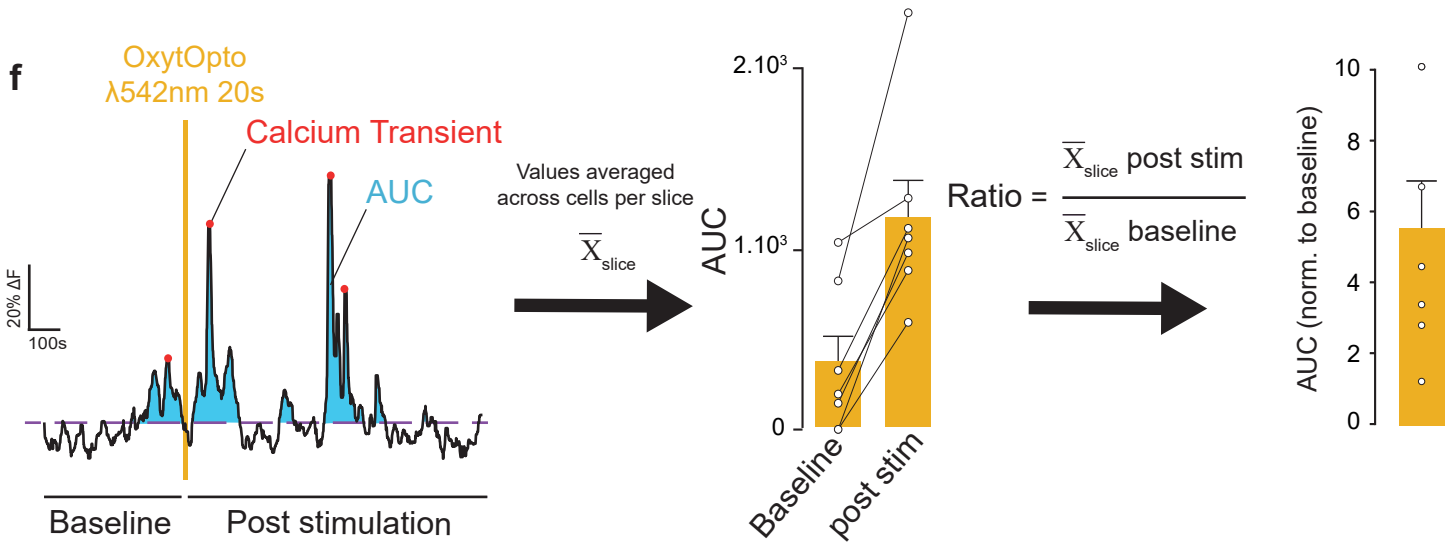
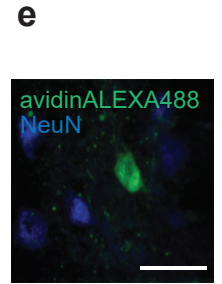
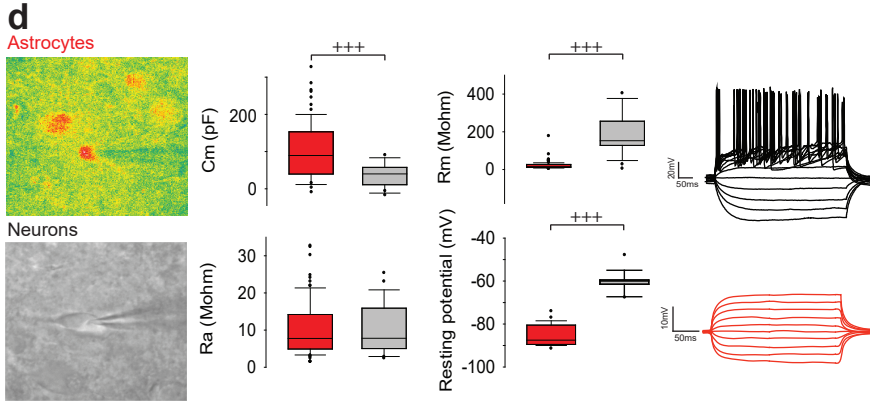
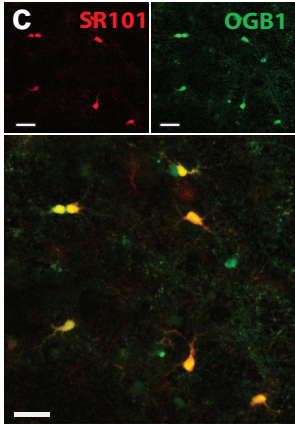
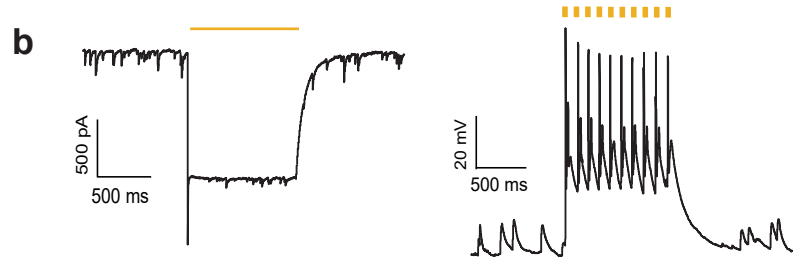
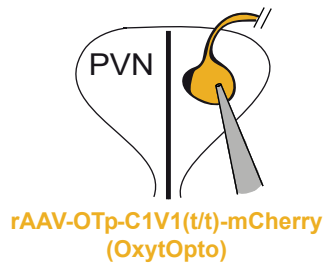
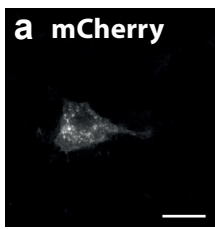
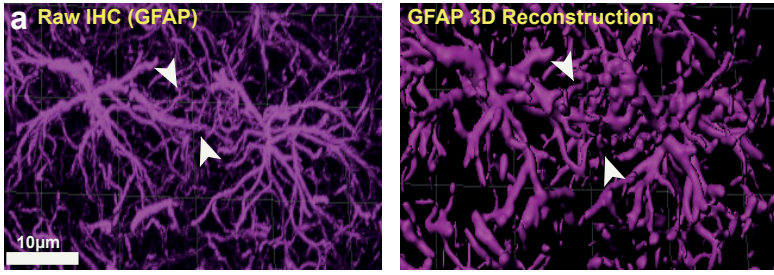


Figure 7

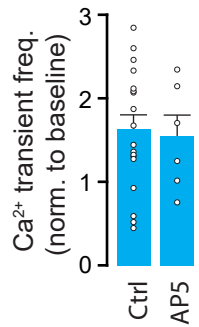
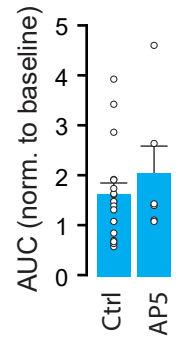
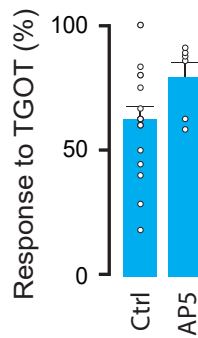
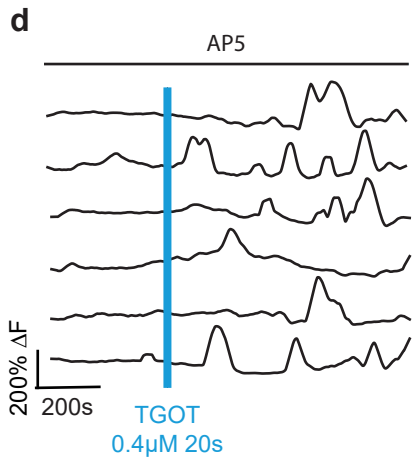
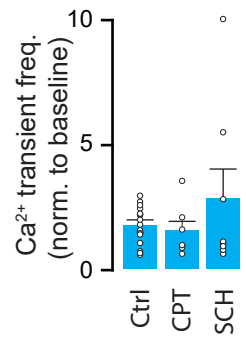
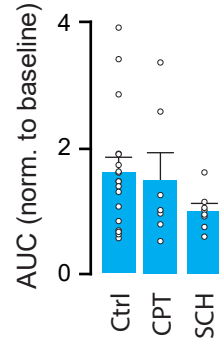
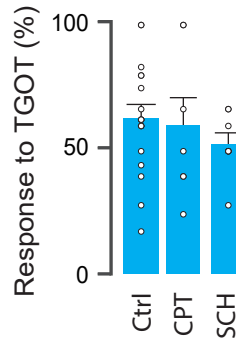
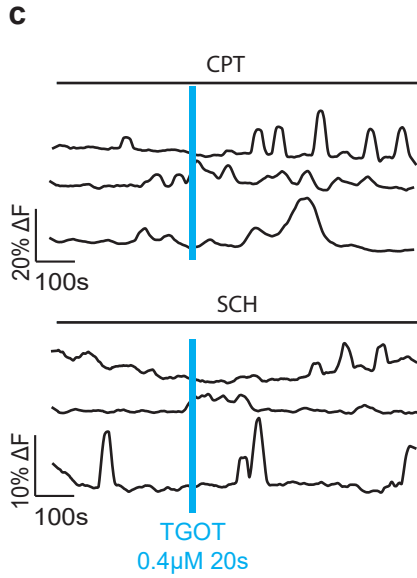
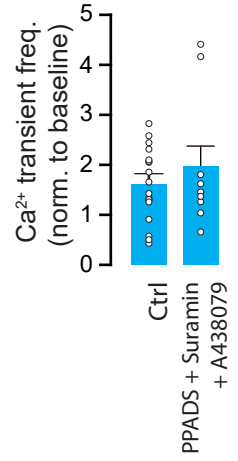
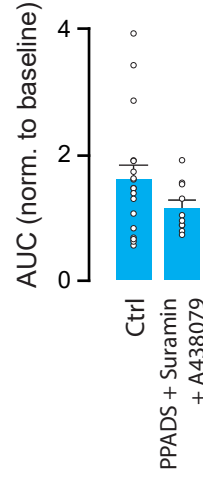
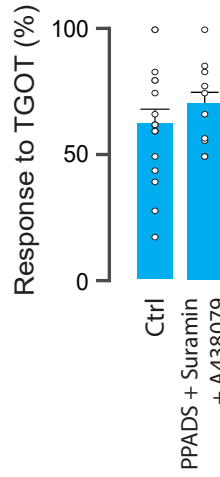
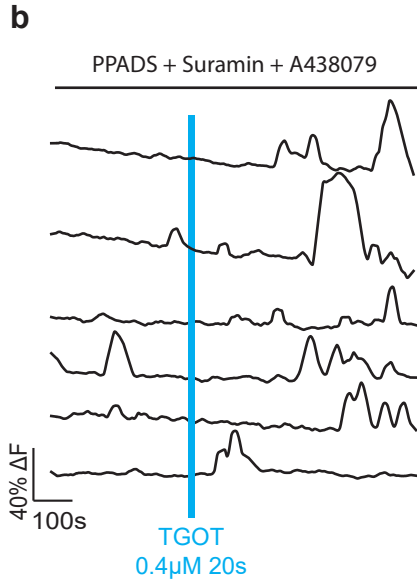


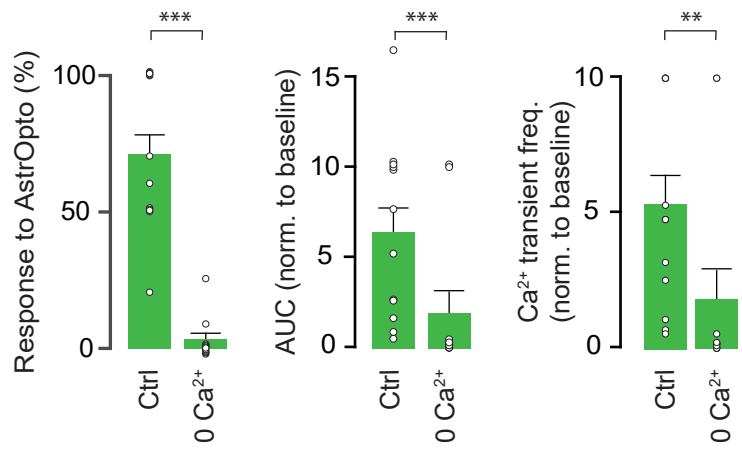
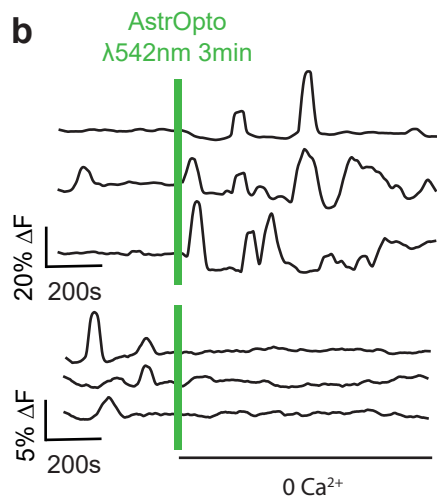
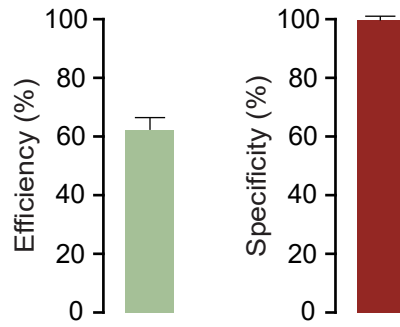
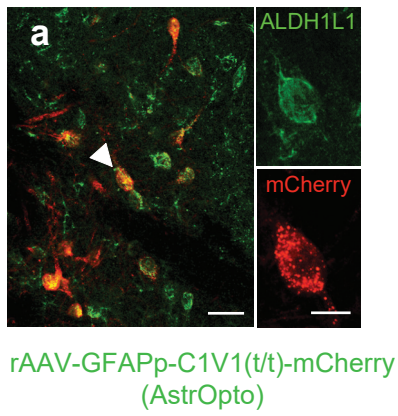
Extended Data Figure 1



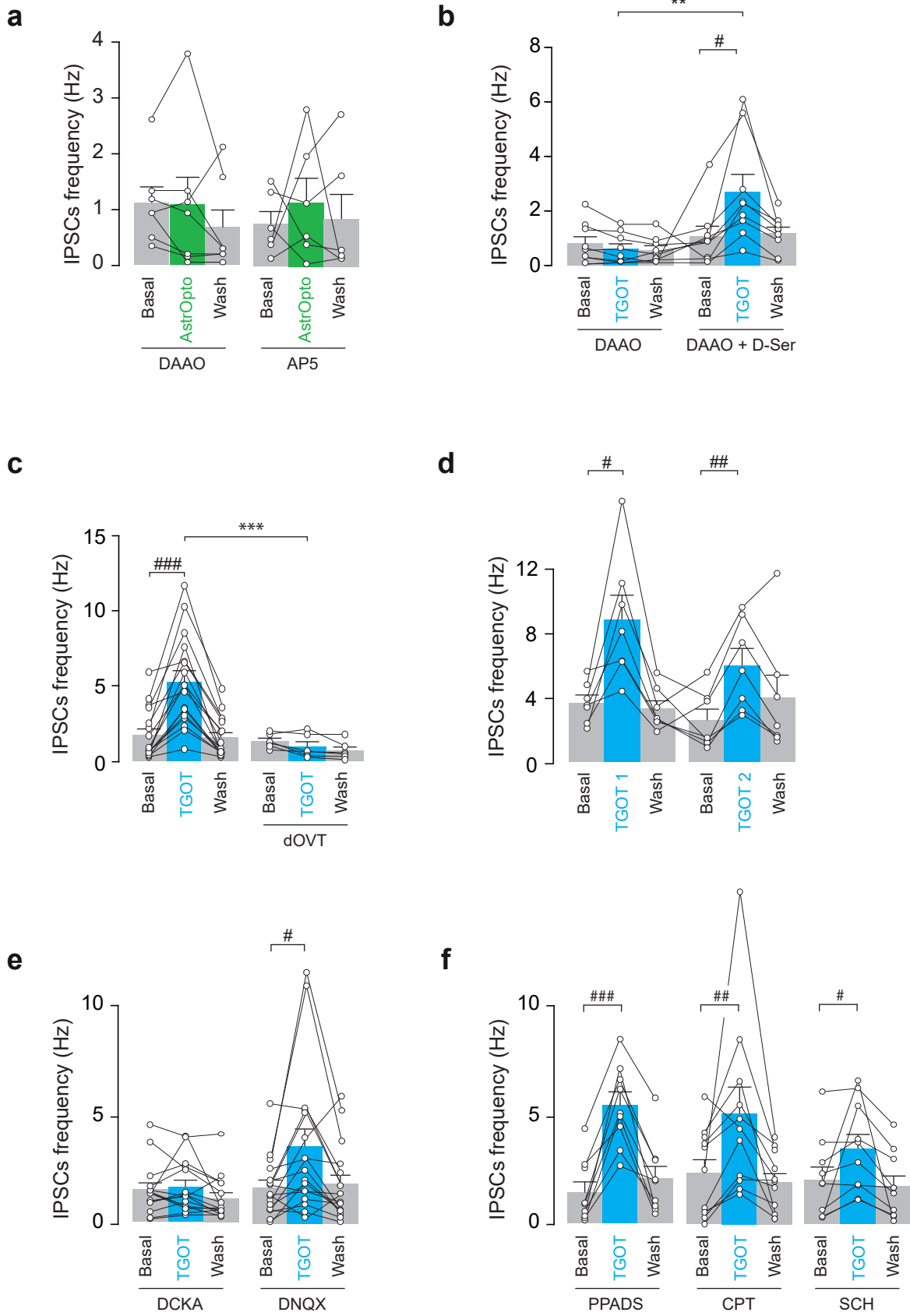


$$\text{Number of contacts} = \sum_{i=1}^n X_i$$

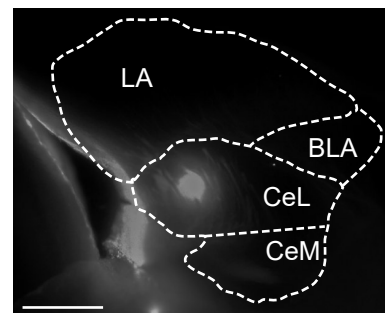
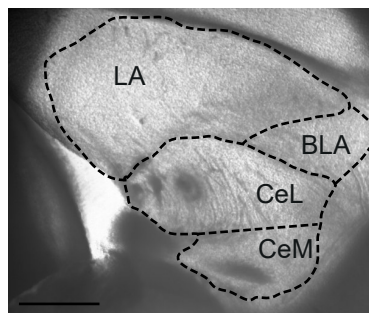
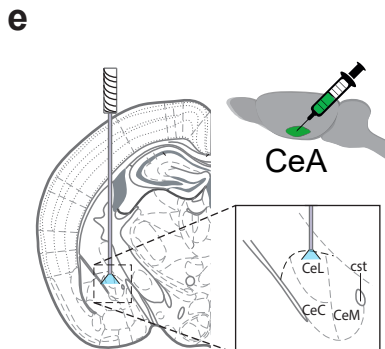
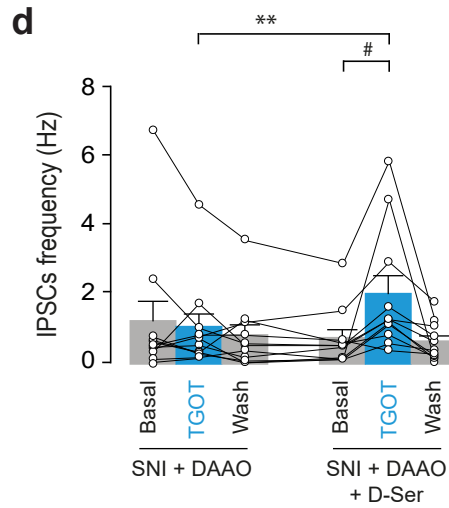
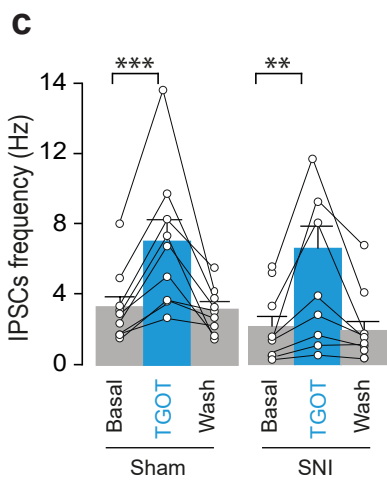
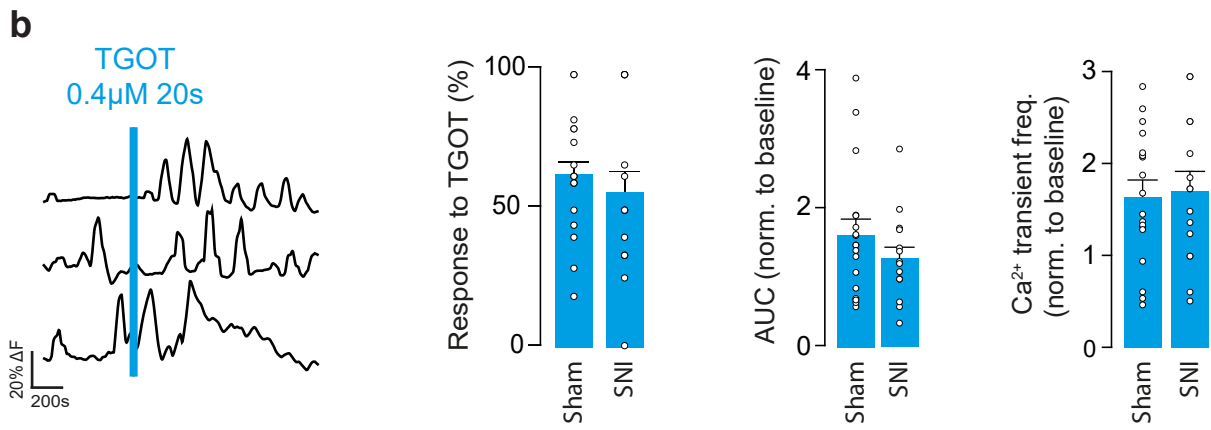
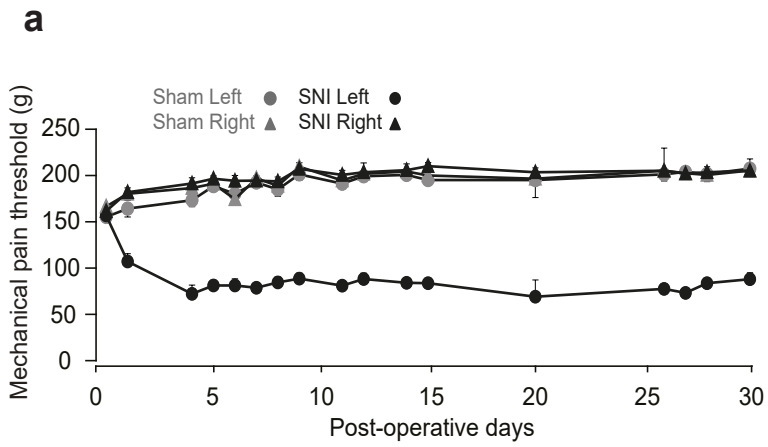




Extended Data Figure 4



Extended Data Figure 5



Extended Data Figure 6

